This work has been submitted to the IEEE for possible publication. Copyright may be transferred without notice, after which this version may no longer be accessible.

# Visual Analysis of Multiple Dynamic Sensitivities along Ascending Trajectories in the Atmosphere

Christoph Neuhauser, Maicon Hieronymus, Michael Kern, Marc Rautenhaus, Annika Oertel, and Rüdiger Westermann

Abstract—Numerical weather prediction models rely on parameterizations for subgrid-scale processes, e.g., for cloud microphysics. These parameterizations are a well-known source of uncertainty in weather forecasts that can be quantified via algorithmic differentiation, which computes the sensitivities of prognostic variables to changes in model parameters. It is particularly interesting to use sensitivities to analyze the validity of physical assumptions on which microphysical parameterizations in the numerical model source code are based. In this article, we consider the use case of strongly ascending trajectories, so-called warm conveyor belt trajectories, known to have a significant impact on intense surface precipitation rates in extratropical cyclones. We present visual analytics solutions to analyze interactively the sensitivities of a selected prognostic variable, i.e. rain mass density, to multiple model parameters along such trajectories. We propose a visual interface that enables to a) compare the values of multiple sensitivities at a single time step on multiple trajectories, b) assess the spatio-temporal relationships between sensitivities and the shape and location of trajectories, and c) a comparative analysis of the temporal development of sensitivities along multiple trajectories. We demonstrate how our approach enables atmospheric scientists to interactively analyze the uncertainty in the microphysical parameterizations, and along the trajectories, with respect to a selected prognostic variable. We apply our approach to the analysis of convective trajectories within the extratropical cyclone "Vladiana", which occurred between 22-25 September 2016 over the North Atlantic.

Index Terms—Meteorology, trajectories, temporal data, multi-parameter data, diagrams, linking, focus+context, sensitivity analysis.

### 1 Introduction

**T** N meteorology, the warm conveyor belt (WCB) is a welldefined moist airstream, which originates in the lowermost levels of the atmosphere within an extratropical cyclone's warm sector and generally ascends poleward to the upper troposphere within two days [1]. WCBs play a critical role in cloud formation and precipitation in the extratropics (e.g., [2], [3], [4]). In numerical simulation output from, e.g., numerical weather prediction (NWP) models, WCBs are typically detected and analyzed by means of path lines (in the atmospheric sciences usually simply referred to as "trajectories") computed from the simulated time-dependent 3D wind field. Domain scientists use coherent sets of trajectories to analyze structures which are not directly visible using the time-dependent 3D fields, such as, e.g., the origins of moist airflow or how precipitation patterns emerge from different trajectory ascent. WCB trajectories are characterized by different ascent rates. The majority of WCB trajectories ascend gradually and slantwise from the lower into the upper

 Christoph Neuhauser and Rüdiger Westermann are with Technical University of Munich (TUM).
 E-mail: {christoph.neuhauser | westermann}@tum.de. troposphere [2], however, faster convective ascent can be embedded. Convective WCB trajectories play an important role in weather forecasting, e.g., since they have a significant impact on intense surface precipitation rates [5], [6], [7].

The scale of cloud microphysical processes, which are responsible for precipitation formation, is too small to be explicitly resolved in NWP models. Hence, parameterizations are used to calculate the integrated effects on the resolved prognostic variables. These parameterization schemes are still associated with large uncertainties that influence, e.g., rain density formation and trajectory ascent. A thorough analysis of the impact of model parameters on, e.g., rain formation and precipitation, can clarify how, when and where trajectories' properties are sensitive to specific parameterized processes.

Algorithmic Differentiation (AD) is a method to compute derivatives of an implemented model [8], which can be used to quantify the impact of multiple model parameters on a prognostic variable at once. AD exploits the fact that any implemented model is a sequence of differentiable, elemental operations on a low level. By repeatedly applying the chain rule, the derivative for any code can be calculated automatically alongside the usual run of the code. AD has been applied on a warm-rain microphysics scheme for idealized trajectories [9], and recently on convective and slantwise WCB trajectories [10]. Sensitivity is defined as the linearly predicted change of a prognostic variable if a model parameter is perturbed by 10%. The prognostic variable can be any of the simulation output, such as temperature or hydrometeor content. The linear prediction is the gradient computed via AD times 10% of the model parameter value.

The application of AD to a prognostic variable along

Maicon Hieronymus is with Johannes Gutenberg University Mainz. E-mail: mhieronymus@uni-mainz.de.

Michael Kern is with Advanced Micro Devices, Inc. E-mail: Michael.Kern@amd.com.

Marc Rautenhaus is with Universität Hamburg. E-mail: marc.rautenhaus@uni-hamburg.de.

Annika Oertel is with Karlsruhe Institute of Technology. E-mail: annika.oertel@kit.edu.

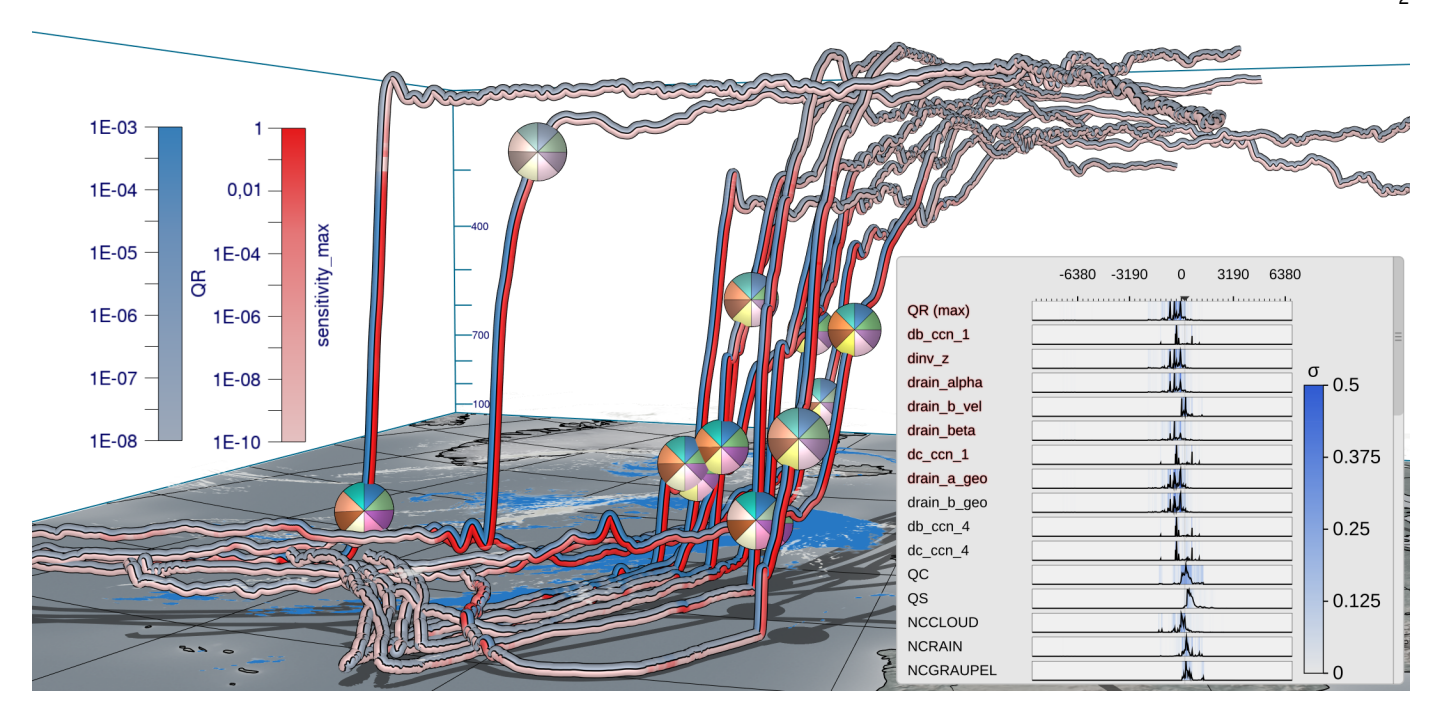


Fig. 1. Visual analysis of the sensitivity of a prognostic variable to selected model parameters (emphasized in red in curve plot overlay) along warm conveyor belt trajectories in the extratropical cyclone "Vladiana", to assess uncertainties of parameterizations in numerical weather prediction models. Prognostic variable (blue) and maximum sensitivity (red) are color coded along the trajectories in bands that are view-aligned, to avoid occlusions that occur when bands are fixed to the trajectory surface. Multiple sensitivities at a selected time step are visualized via pie charts that are mapped onto spheres in the 3D view. A consistent view-aligned mapping of sensitivities to pie charts enables an effective comparison across the trajectories. Embedded curve plot shows statistical summaries of prognostic variables, sensitivities, and model parameters to which sensitivities are computed. Surface precipitation is shown on the ground in blue.

WCB trajectories results in one sensitivity value of this variable for each model parameter and on each simulation point along the trajectories. We build upon the work by Hieronymus et al. [10], who provide a tool and data to analyze microphysical sensitivities in a WCB case-study by means of statistical approaches. Sensitivities along trajectories are analyzed by plotting time-curves and manually comparing the curves associated to different model parameters. The spatial and temporal behavior of sensitivities along individual trajectories or groups of trajectories has not been considered. Oertel et al. [5] show that large spatio-temporal variability in terms of trajectories' ascent and characteristics exists - to which extent this also applies to sensitivities remains an open question and motivates the study at hand.

In our application, trajectories are calculated from the resolved 3D wind field using the online trajectory module [11] in COSMO. Every 2h, multiple trajectories are started from a predefined starting region at seven vertical levels. The sensitivities are then calculated by re-simulating the microphysics along slantwise and convective ascending trajectories from this set. Hence, analysis of such data requires more sophisticated visualization approaches than standard techniques. In particular, through the sustained collaboration between experts from the fields of visualization, computational science and meteorology in the scope of the "Waves to Weather" Transregional Collaborative Research Project<sup>1</sup>), the following questions have turned out to be of considerable relevance to meteorologists:

Q1 Do similar trends regarding selected sensitivities and

prognostic variables occur across a group of selected trajectories?

Coherent trajectory clusters are often characterized by specific properties relevant for process understanding in atmospheric sciences. So far, the similarity of certain properties of pre-selected trajectory groups has been mostly plotted manually as individual sub-panels [2], [12].

- Q2 Do different sensitivities and prognostic variables show similar statistical characteristics across a selected trajectory group?
  - Similarities of trajectory properties provide insights in process understanding. So far, correlations are mostly identified based on individually calculated correlations or based on visual analysis.
- Q3 How do sensitivities depend on the time and location along the trajectories, and how are they related to, e.g., surface precipitation and cloud formation? Detailed process understanding requires the current atmospheric state, which is why the combination of trajectories with 3D NWP output is very useful.
- Q4 Do coherent sensitivity patterns emerge if trajectories ascending at different times are considered relative to their time of ascent?

In atmospheric sciences, coherent airstreams related to specific weather phenomena can be identified based on their spatio-temporal evolution, such as, for example, strong ascent or descent. Thus, their common characteristics are most pronounced if the trajectories' properties are centered relative to their coherent evolution (e.g., Oertel et al. [5]), which in

this case-study is the time of the WCB trajectories' ascent start.

Q5 Do sensitivities differ with respect to different types of trajectories (i.e., convective vs. slantwise)?

Although pre-selection of trajectories often results in coherent trajectory clusters, their detailed characteristics still often differ substantially which typically needs to be analyzed based on pre-defined criteria.

An intuitive analysis of these aspects will enable domain scientists to further investigate the uncertainties in the employed numerical models - which is much needed for further improvement of NWP models.

Contributions. We propose a visual analytics workflow combining novel application-specific and standard visualization techniques to answer the raised questions. The workflow embeds a curve plot view into a 3D trajectory view and links these two in a bidirectional way. For display in the 3D view, the user selects a prognostic variable, i.e., the target variable, and a set of sensitivities, and can now interactively select time points at which the sensitivities are visualized.

To address Q1, we provide a multi-parameter curve plot showing the time evolution of the maximum and standard deviation (stdev) to this maximum over all trajectories for any selected sensitivity. Q2 is resolved by automatically sorting sensitivities according to the similarity of their temporal development to a selected sensitivity. In addition, the user can select a short-term trend in the curve plot of a sensitivity and let the system search for similar short-term trends in the temporal developments of other sensitivities. The curve plots view enables an interactive comparative visualization of the statistical similarities of local and global trends in the temporal evolution of sensitivities across the set of selected trajectories. Likewise, the trend analysis can be performed for other prognostic variables and model parameters, then showing the mean and stdev to the mean.

While Q3 can be partially answered via the curve plots, this view cannot reveal the relationships to the locations and shapes of the trajectories and surrounding atmospheric fields. Therefore, the curve plots view is embedded into Met.3D, an open-source 3D visualization system dedicated to meteorological analyses [13]. Met.3D visualizes the trajectories in their spatial context (i.e., the 3D trajectory view), including visualizations of additional data sources like textured terrain fields, and in particular 3D atmospheric field data. In principle, Q3 can then be addressed by showing multiple sensitivities along a trajectory via colored bands. This, however, becomes unsuitable as soon as more than 2-3 sensitivities are visualized simultaneously, because the single bands become too thin and can hardly be distinguished. Therefore, we propose a visual mapping using enlarged spheres, which can be moved along the trajectories to specific time points and, due to their extended surface area, can effectively show more bands simultaneously. To also use the trajectory surface for conveying information, the target variable and the maximum sensitivity over all trajectories at each time step are shown via two colored bands along the trajectories. We introduce view-aligned bands, to avoid occlusions that occur when bands are fixed to the trajectory surface. By automatically determining for each trajectory

its unique time of ascent and interpreting the current time relative to this times, differences and similarities in the sensitivities during the ascend phases can be revealed (to resolve Q4).

The 3D view shows at a glance whether the sensitivities selected for visualization are similar or dissimilar across the set of trajectories. However, since the bands on a sphere are aligned with the trajectory, the bands' orientations vary across the set of trajectories so that a comparative visual analysis becomes difficult. To overcome this limitation (to resolve Q5), we propose to graphically depict the sensitivities via a pie chart that is consistently oriented in view-space and mapped onto the spherical shape. We assess the effectiveness of both visual mappings via a user study.

The specific contributions to solve questions Q1 to Q5 are:

- A tube-based trajectory view showing the trajectory data in its geospatial context, using view-aligned color bands on each tube to avoid occlusions and twists
- A sphere-based focus view acting both as a time step marker and magnifying lens. It encodes multiple sensitivities via view-aligned bands or pie charts to enable an effective comparison of the sensitivities on different trajectories.
- A curve plots view showing statistical summaries of prognostic variables and sensitivities, which provides options to automatically sort the individual plots according to similarity and occurrence of userselected subsequences.

The remainder of this paper is structured as follows. After reviewing work that is related to ours in Sec. 2, we provide an overview of the proposed workflow, including a description of the input data and visualization options. In Sec. 4, we introduce the design and functionality of the curve plots view and the 3D trajectory view. A description of the technical realization of both views is given in Sec. 6. Fig. 12 demonstrates the application of the proposed workflow to analyze convective trajectories within the extratropical cyclone "Vladiana". We conclude the paper with a summary of our main contributions and ideas for future work.

#### 2 RELATED WORK

The workflow and techniques we propose are related to multi-parameter and ensemble visualization techniques, as well as feature-based visualization in meteorology.

Multi-Parameter and Ensemble Visualization. In the curve plots view, we use simple statistical summaries to quantify the spread of variables and sensitivities across a set of trajectories [14], [15]. Previous works in ensemble visualization have proposed more advanced graphical depictions to visually convey the ensemble spread of scalar and vector fields (see the survey by Wang et al. [16] for an overview), and research has been pursued regarding visual abstractions of the major trends in ensembles of line and surface features [17], [18], [19]. This is different from our application scenario, where the spread of scalar sensitivities

across a set of 3D lines is to be analyzed. This requirement also distinguishes from approaches that represent the spread in ensembles of multi-dimensional scalar fields, for instance, via histogram encodings [20], linearized spatial representation using bar charts [21], or probability density functions and distributions [22], [23], [24], [25], [26].

Furthermore, since we are dealing with trajectories in 3D space, stacking-based trajectory visualization as, e.g., proposed by Tominski et al. [27], is unsuited for reaching our goals. Such approaches visualize a set of 2D trajectories by stacking them on top of each other as bands along which attributes are encoded via color. However, since the trajectories we consider live in 3D space, stacking is impossible without projecting the trajectories into a common 2D space where shape information is lost. Composite density maps [28] or visitation maps [29], on the other hand, aggregate 2D or 3D trajectories depending on specific attributes or shape similarities. Since such techniques do not allow distinguishing individual trajectories, they become inappropriate in our application scenario.

Instead of curve plots as in our workflow, violin plots [30] could be used in principle. Violin plots have been proposed for location-based time-series visualization [31], [32]. Recently, they have been extended to compare multiparameter data across a set of simulation ensembles [33], by showing the histograms of many parameters simultaneously on both sides of a vertical center line. Multi-parameter violin plots can be used in our scenario to show side-by-side the temporal evolution of multiple parameters along the trajectories. On the other hand, for the possibly many trajectories we have, the visualization becomes quickly overloaded and requires significantly more space than the statistical summary visualizations used in this work.

Parallel coordinate plots [34], [35] are another option to directly visualize large sets of multi-parameter data points in a single view. A multitude of methods have been proposed to improve the visibility of single data points in such plots. The survey of Heinrich and Weiskopf [36] discusses many of these improvements. Parallel coordinate plots, however, are problematic in the current scenario, since it becomes difficult to differentiate the data points belonging to different trajectories and convey the temporal evolution of the sensitivities. Furthermore, information about the location and shape of the trajectories along which sensitivities are analysed is difficult to integrate.

Regarding its goals, our proposed approach also shares similarities with techniques that are used to investigate the relationships between multiple input parameters and a single simulation output parameter [37], [38], [39], [40]. These approaches do not visualize sensitivities directly, but they visualize the changes in a simulated phenomenon, like a flow field, due to variations in the input configurations. Thus, they work with an ensemble of simulation runs, while underlying our approach is the existence of a single multiparameter simulation on an ensemble of paths through the atmosphere.

Closest to our approach regarding the visualization of quantities along trajectories in 3D space is the technique proposed by Sadlo et al. [41] for visualizing the transport of vorticity along such trajectories. They introduce striped pathlines and slices along the trajectories with extended

radius to encode vorticity-specific information. Both the stripe pattern as well as the slices repeat in discrete steps along the trajectory, so that values can be missed. The proposed coloring also has the problem that the stripes become thinner or thicker depending on the bending of a trajectory. Due to the orientation of slices orthogonal to the trajectory tangent, the coloring on these slices is obscured when viewing trajectories from the side.

Feature-based Visualization in Meteorology Our driving science domain in this study is meteorology. Meteorological applications have frequently motivated work on visualization in recent years. Overviews were provided by Rautenhaus et al. [42], Azfal et al. [43] and Yohizumi et al. [44]. Different aspects of visualization in meteorology have been addressed, including feature-based visualization, flow visualization and 3D interactive visual analysis techniques, all relevant to the techniques discussed in our work. Recent examples in the literature include 3D visual analysis of severe weather (e.g., of supercell thunderstorms [45] and polar lows [46]), and feature-based (mostly 3D) techniques to track cyclone paths [47] as well as more generic scalar extremal features [48], and to analyze potential vorticity banners [49], jet stream flow [50], [51], atmospheric fronts [52], and -as in this study- WCB trajectories [53]. Visual analysis of simulation uncertainty in meteorology has mostly been addressed in the context of visualizing output from simulation ensembles [16], [42], e.g., to characterize uncertainty in NWP with respect to uncertainty in initial values. In contrast, in our work, uncertainty information is computed by means of algorithmic differentiation to yield sensitivities with respect to parameters in a numerical simulation.

Algorithmic Differentiation. Algorithmic Differentiation (AD) is used to compute derivatives of a given computer code in an automatic way [8]. It has been previously used for sensitivity analysis of the MM5 mesoscale modeling system to evaluate the impact of additional observations on the initial temperature field [54]. Baumgartner et al. [9] applied AD for a sensitivity analysis along idealized trajectories and warm cloud microphysics. Other use cases include optimization problems, such as optimizing model parameters in machine learning, e.g., in PyTorch [55], or applying gradient descent or Newton's method [56]. Typical test cases for AD tools include numerical optimization for partial differential equations, i.e., solving Reynolds Averaged Navier-Stokes equations [57].

### 3 Workflow Overview and Data

The proposed workflow and methodology enables meteorologists to interactively analyze the effects of simulation model parameters on a selected target variable. We apply it to rain mass density along convective warm conveyor belt trajectories, which are responsible for heavy rainfall on the earth surface. The analysis hints on relationships between the trajectories' spatial locations and shapes, and the occurrence of specific features in the sensitivities of the selected variable to different model parameters. From its existing support to display a single parameter along 3D trajectories [53], Met.3D has been extended according to the specific visualization options required to support a comparative analysis as mentioned.

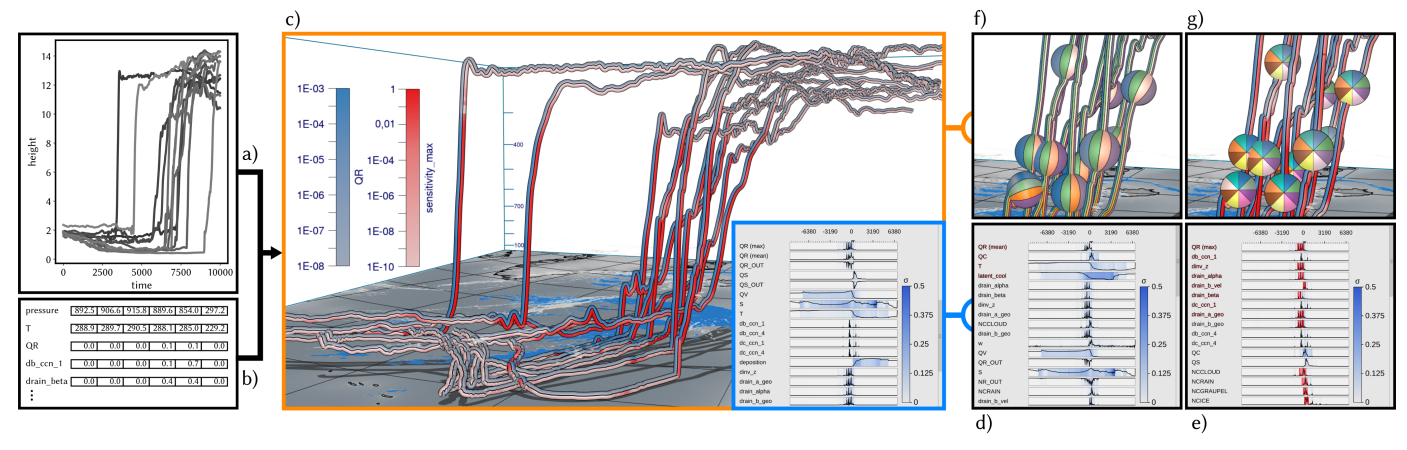


Fig. 2. Workflow overview: Met.3D reads a) 3D trajectory data and b) tables of model variables and sensitivities along the trajectories. c) The visualization canvas of Met.3D, including the 3D trajectory view that is linked to the curve plots summary view. d) Statistical summaries of the temporal development of variables and sensitivities, which can be ordered automatically regarding the similarity of their temporal development to a selected variable or sensitivity. e) Variables exhibiting a selected sequence of events can be determined automatically and shown first. f) and g) Focus view options using sphere-based multi-parameter visualization via view-aligned bands and pie charts.

Fig. 2 shows an overview of the workflow. The input (Fig. 2a) is a set of convective WCB trajectories which have been computed over a time interval of interest, and a set of model parameter sensitivities along these trajectories with respect to a selected prognostic variable (Fig. 2b). Sensitivities are named "d[...]", which stands for  $\partial QR/\partial$ [...], where rain mass density (QR) is the selected target variable, and "[...]" is the model parameter in question. "sensitivity\_max" is the per-time maximum of all sensitivities. We consider WCB trajectories that are computed for the extratropical cyclone "Vladiana", which developed from 22-25 Sep 2016 in the North Atlantic during the North Atlantic Waveguide and Downstream Impact Experiment field campaign [58] The trajectory data of the case-study shown here is taken from a simulation described in detail by Oertel et al. [5] with the NWP model COSMO version 5.1 [59]. In addition, an online trajectory scheme [11] was applied to calculate the positions and properties of the trajectories from the resolved 3D wind field at every model time step, here 20 s.

AD has been applied to convective and slantwise trajectories in "Vladiana" with the tool from [10], which implements the Seifert and Beheng two moment cloud microphysics model [60] including routines for the ice phase [61], [62] and augmented with CoDiPack [63] to evaluate the Jacobian of the implemented model at every time step in an efficient way. Overall, the sensitivities of rain mass density with respect to 177 model parameters have been computed via AD, of which the 40 most important parameters are used in this work.

The user first inspects the parameter sensitivities by means of curve plots which are shown as overlays in Met.3D (blue outline in Fig. 2c). Curve plots show the temporal development of statistical summaries over the set of trajectories (i.e., the maximum and stdev to the maximum) of the target variable and sensitivities. To enable a comparison of different prognostic variables, their means and stdevs to the mean can be shown in the curve plots as well. Initially, the target variable is shown on top, and all sensitivities and other variables are shown below it in random order. Both the sensitivities and variables can be sorted with respect to the similarity of their temporal development to

a user-selected sensitivity or variable (cf. Fig. 2d), and those whose curve contains a temporal pattern that is similar to a user-selected pattern can be determined automatically and shown together (cf. Fig. 2e).

The initial inspection is used to quickly obtain an overview of the temporal behavior of the variables and sensitivities. It shows when and for which model parameter high sensitivities occur, and which sensitivities or prognostic variables show a similar temporal development.

In the 3D view of Met.3D, all trajectories are rendered as tubes (orange outline in Fig. 2c). Additional visualizations of the earth surface and shadows place trajectories in spatial context. Along each tube, two colored bands are used to visualize the target variable and one other quantity. For close-up views, more bands using a selected set of parameters can be shown (cf. Fig. 12). Per default, the maximum of all sensitivities is mapped to the second color, to indicate locations of possibly high uncertainty, i.e., high effect of a small change in the model parameter on the selected variable.

The curve plots view is linked to the trajectory view in that the user can move a vertical line along the time axis, and instantly the points on each trajectory corresponding to that time are highlighted by a focus view. The focus view comprises a spherical glyph that is centered at the tube and colored via bands (cf. Fig. 2f) or a pie chart (cf. Fig. 2g), both encoding multiple sensitivities simultaneously .

The number of bands to be shown and the number of subdivisions of the pie chart is given by the number of sensitivities the user selects. Both bands and pie charts are aligned consistently in view-space to allow for an effective visual comparison of the shown values across the trajectories. Within each pie chart, the selected sensitivities in top to bottom order in the curve plots view are mapped to pie chart pieces in clockwise order. In Sec. 4.2, we discuss the different visual designs.

Alternatively to moving the time line in the curve plot, the user can pick a sphere glyph and move it along the trajectory. All other glyphs are moved accordingly in time so that via animation the sensitivities on different trajectories can be compared (cf. supplementary video).

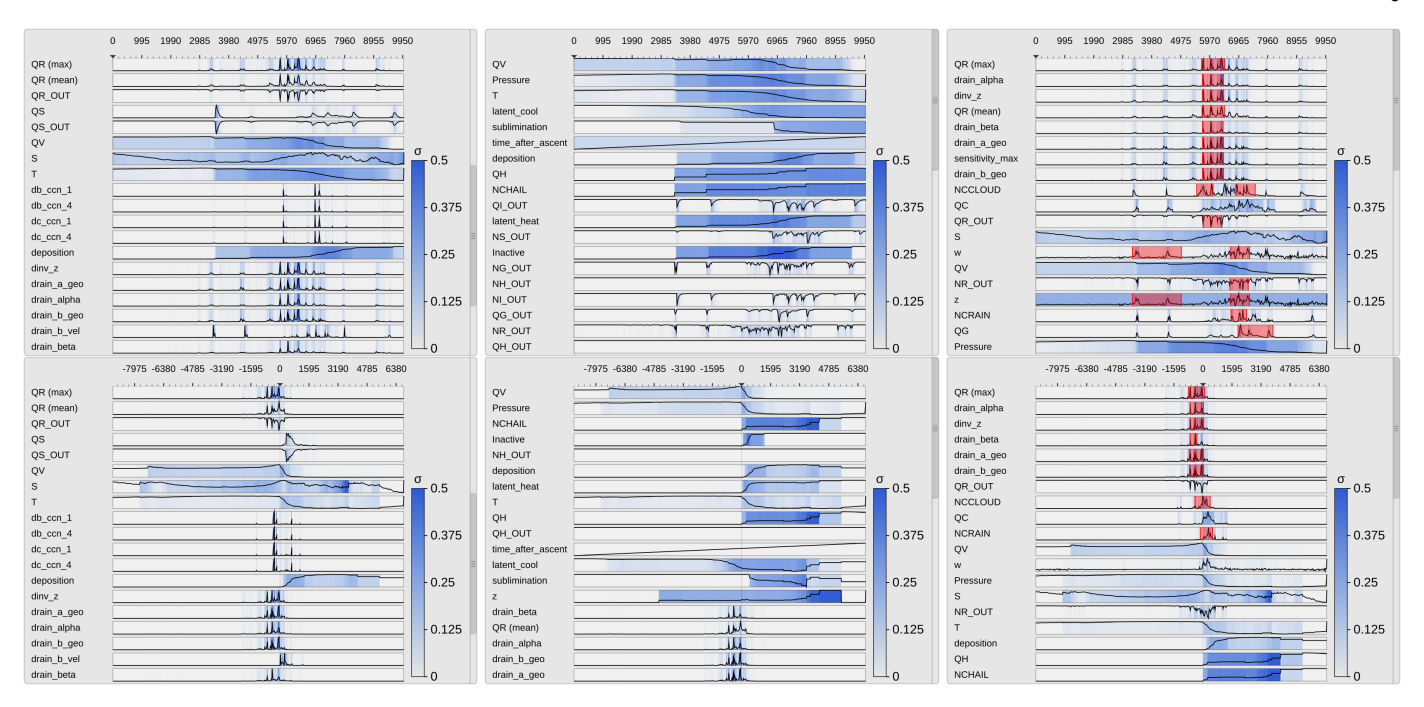


Fig. 3. Curve plots with trajectories aligned by time step (top) and time of ascent (bottom). Curve plots show the mean of prognostic variables and the maximum of sensitivities over all trajectories with color encoded stdev to the mean/maximum. Top band shows target variable rain mass density (QR). Left: Curve plots in random order. Middle: Curve plots are sorted regarding the similarity of their time development relative to the target variable QV (cloud mass density). Right: Sorting regarding similarity to max QR. A pattern of consecutive spikes has been selected in QR, and regions in which similar features have been determined are highlighted.

### 4 VISUALIZATION TECHNIQUES

The visualization workflow presented in this work builds upon a curve plots view, a 3D trajectory view, and interactive linkage between these two views. Linkage enables to find relationships between locations with high sensitivities along trajectories and the trajectories' locations and shapes.

### 4.1 Multi-Parameter Curve Plots View

The curve plots view shows the single curve plots of the prognostic variables and sensitivities vertically aligned (cf. Fig. 3). The time axis is going to the right and the vertical axis represents the value domain. All values are initially normalized to [0,1]. The trajectories are traced with a time step of  $\Delta t = 20s$ , which is also the time delta between two data points in the horizontal axis. When the number of time steps exceeds the number of pixels reserved for showing the curve plots, the algorithm largest triangle three buckets (LTTB) [64] is used to recursively downsample the data. LTTB takes into account the perceptual importance of points during the downsampling process by assessing the area of triangles formed by points in neighboring buckets. In this way, the performance penalty of drawing too many points can be avoided, simultaneously ensuring that no features are lost. By generating the curve plots at multiple resolutions, the user can zoom into interesting time intervals and analyze the variables and sensitivities over these intervals in more detail.

For the target variable and sensitivities, in each band the maximum over all trajectories is shown via a curve. For all other prognostic variables and model parameters the mean over all trajectories is shown. Since the sensitivities are often close to zero, resulting in very small mean values, the maximum values and corresponding stdevs can far more effectively indicate the spread of the distributions and the overall trend regarding their strengths. In particular, regions of potential local instability are emphasized and high sensitivities aren't missed. The background is colored according to the stdevs with respect to the values represented by the curves, i.e., stdev is mapped to a color ranging from white (low value) to blue (high value). By utilizing mouse controls, the user can scroll through the set of parameters and zoom into individual regions in the curve plots view. A moveable vertical line indicates the currently selected time step.

Since there are many parameters and not all can be shown in one single view, the system proposes an automatic ordering to quickly identify sets of parameters with similar sensitivity development over time. Therefore, the user selects an individual curve plot, and the system sorts all curve plots in descending order regarding the similarity to the curve in this plot. As a measure of similarity we use the absolute normalized cross-correlation

$$NCC(X,Y) = \frac{1}{N} \sum_{i} \frac{(X_i - \mu_x)(Y_i - \mu_y)}{\sigma_x \sigma_y}.$$
 (1)

Here,  $X_i$  and  $Y_i$  are two time series, and  $\mu_x, \mu_y$  and  $\sigma_x, \sigma_y$  the corresponding means and stdevs. Note that due to the division by the stdev, A NCC becomes independent of the scale of the two time series.

We further considered CrossMatch [65] and the "edit distance on real sequence" (EDR) [66] as alternatives for similarity sorting. However, since the former does not support data normalization, and the latter may suppress relevant sensitivities due to built-in noise suppression, both turned out to be less effective in our scenario.

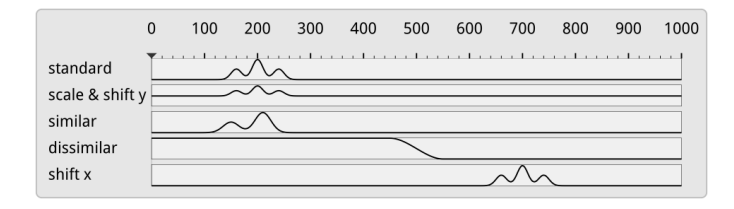


Fig. 4. Test sequences sorted by their similarity to "standard" using the absolute NCC. The NCC can deal with scaling and shifting in the data axis, but not with shifting in the time axis. We address this limitation by aligning curves relative to the time of ascent of the corresponding WCB trajectories.

Fig. 3 left and middle show, respectively, the initial curve plots using a random ordering of variables, and the ordering with respect to the selected temporal distribution of the variable QV. Fig. 3 right shows the ordering with respect to QR. As can be seen, a number of sensitivities behave very similarly to QR and, in particular, show a significant change at the point in time where QR changes significantly. Note here that by using the absolute value of the NCC, it is ensured that parameters with high negative correlation are shown before those with low absolute correlation.

A limitation of NCC is that time series which show a similar but time-shifted behavior are found to be dissimilar (cf. Fig. 4). Even though this can be avoided by computing NCC for successively delayed versions of the original series and finding the peak in the sequence of similarities, we provide a different alternative that takes into account that it is in particular the ascent phase of a trajectory which is of interest. We define the start of the ascent of a trajectory as the start of the most rapid ascent within a 2h window. This is calculated by using a sliding window of 2h and calculating the total ascent within this time window. Finally, the trajectories are shifted in time so that they all start their ascent at the same time, and the shifted versions are then sorted via NCC.

To facilitate an improved comparative analysis of the sensitivities along multiple trajectories, it is furthermore important to find similar reoccurring subsequences in this data. In particular, since trajectories are seeded at different locations and times, they can first travel close to the surface over different time intervals, before similar upstream paths are observed along which specific sensitivity patterns occur. To determine similar patterns, the user can select a time interval using the mouse, and automatically the subsequence of sensitivity values within this interval is searched in the same and all other curves via the subsequence matching algorithm SPRING [67]. SPRING selects all subsequences with a dynamic time warping (DTW) distance less than a user controlled threshold, by warping one sequence so that it best matches another sequence (see Fig. 5 for a schematic illustration). The DTW distance is the sum of the perelement distances of two such optimally aligned sequences. When searching for all subsequences in a sequence of length n with respect to a query sequence of length m with a DTW distance less than a user-specified threshold, a naive algorithm has a time complexity of  $O(n^3m)$ . Due to its time complexity of O(nm), SPRING enables interactive use even for long sequences.

As SPRING is based on dynamic time warping, the time

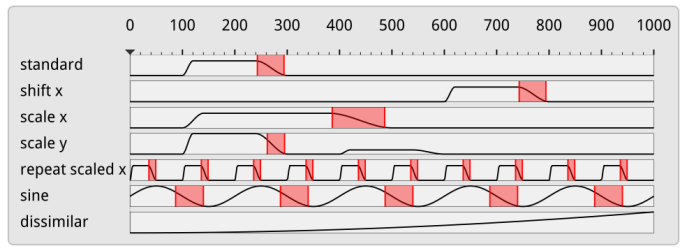


Fig. 5. Subsequence matching in the curve plots view using SPRING. SPRING, due to dynamic time warping, can pick up patterns that are shifted and scaled in the time axis.

scale of subsequences may be both stretched or compressed. As can be seen in Fig. 3 right, this enables to select, e.g., all falling edges in the temporal developments, independently of their duration. The found subsequences are underlined by red background color. Compared to NSPRING [68], an extension of SPRING that adds support for data normalization, in all of our experiments SPRING gave most plausible results in line with our perception of similarity (i.e., that the similarity of two sub-sequences is also dependent on their scale).

### 4.2 Trajectory View

In the trajectory view, all given trajectories are shown in their geospatial context using Met.3D (cf. Fig. 2). Each trajectory is rendered as a colored and illuminated tube with black outlines to let it stand out against the background. Per default, the target variable and the maximum sensitivity are encoded by two different colors, and they are shown on the tube via two bands running into the direction of the trajectory's tangent (see Fig. 6a for an illustration).

However, when defining these bands in object space, i.e., the assignment of points on the tube surface to either band is fixed, parts of a band can disappear and become visible on the opposite surface part when rotating about the trajectory or when the tube twists. This makes it difficult to match a band with its corresponding quantity, and it is especially critical when multiple trajectories are shown and need to be compared regarding the data that is shown in the bands. To avoid this problem, we have developed a rendering technique that renders the bands so that each band covers always one half of the visible tube surface regardless of the current view and the tube's orientation (cf. Fig. 6b). This rendering is used in all trajectory views throughout this work.

While in principle it is possible to show more than two bands on each trajectory, quickly with increasing view-distance the bands cannot be distinguished anymore. To circumvent this restriction, we propose a focus view that utilizes a locally enlarged surface to obtain more space for the shown sensitivities. On each trajectory, a sphere with adjustable radius is rendered at the currently selected time. The sphere acts both as a time marker and a magnifying glass enabling the display of more sensitivities at once. By showing the focus sphere on each trajectory only at the selected time, occlusions that are introduced when increasing the radii of the trajectories everywhere can be avoided. Initially, only the two bands along the trajectory tubes are continued over the sphere (cf. Fig. 6b).

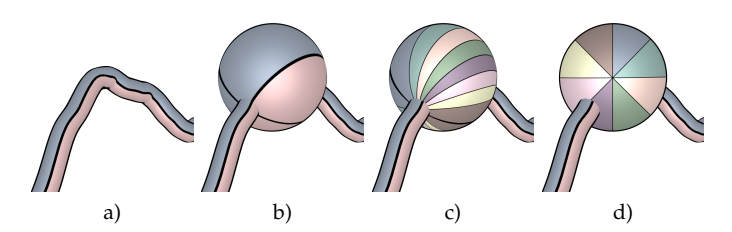


Fig. 6. a) Target variable (bluish colormap) and maximum sensitivity (reddish colormap) are mapped to bands along a tube's surface. b) A focus sphere is used to increase the area on which sensitivities are encoded. c) Multiple sensitivities are mapped to bands running along the trajectory and across the sphere's surface. d) Multiple sensitivities are displayed via a pie chart that is mapped onto the sphere surface.

To show more than two sensitivities on a focus sphere, we introduce two different visual mappings. The first mapping acts like a magnifying glass when multiple sensitivities or variables were encoded via bands on the tube and continued across the sphere (cf. Fig. 6c). When crossing over the sphere, the bands become wider so that the different colors can be better perceived and distinguished. As for the bands on the tube, also the bands crossing over the sphere are view-aligned, i.e., while they orient according to the trajectory tangent they cover the same parts of the visible sphere surface. In Sec. 6, the rendering approach that is used to generate this view is explained in detail. The advantage of this mapping is that the alignment of the bands with the trajectories gives a visually smooth and fairly uncluttered appearance. On the other hand, due to the illumination of the sphere surface, towards the silhouettes the bands become darker so that the relationships between colors and sensitivities are disturbed. We counteract this by reducing light-dependent shading of the bands, i.e., the coefficients of the Blinn-Phong shading model are reduced for diffuse and specular lighting, while being increased for ambient lighting. Nevertheless, since at some time steps spheres can become positioned at trajectory points with vastly different tangents, a visual comparison of the seen band patterns which are then differently oriented — becomes difficult.

The second mapping intends to avoid the aforementioned drawbacks by using a coloring that neither mimics the use of bands nor is aligned with the trajectory. Our proposed solution is the use of a pie chart-based coloring of the sphere, with each piece given equal area and colored according to a certain sensitivity (cf. Fig. 6d). The values are taken at the selected time step from the trajectory and used to color the pie pieces. The user selects the sensitivities to be shown on the pie chart, and the pie chart is automatically subdivided into an equal number of pieces. Also the pie charts are view-aligned, i.e., they are aligned with the view up-axis (cf. Sec. 6). As for sphere coloring using bands, N best distinguishable colors are chosen from the Brewer colormap [69]. Per default, we offer users the 8-class Set1 qualitative color map from ColorBrewer plus turquoise. Sensitivities from low to high are mapped from 20% saturated to fully saturated colors. This avoids that adjacent pieces with low sensitivities fade out to almost indistinguishable colors. Since each piece of a pie chart is equally affected by shading, the use of shading is less problematic than for bands. Furthermore, each view-aligned chart has a consistent orientation, which makes it easier to compare charts on multiple trajectories. A disadvantage is that pie charts might seem to stand apart from the trajectories, since they are not aligned with their tangents.

### 5 USER FEEDBACK AND STUDY

According to our collaborators from computational science and meteorology, questions Q1, Q2 and Q4 can be effectively resolved by the curve plots view, which has been designed specifically to answer these questions. Due to the possibility to show statistical summaries side-by-side for many sensitivities, in combination with similarity sorting and subsequence matching, large numbers of sensitivities can be handled in a fairly efficient and effective way. The number of sensitivities that can be read by the system is not limited, yet beyond a certain number the corresponding curve plots cannot be shown simultaneously and the user needs to scroll through them. However, especially in this case the functionality of the system allows quickly identifying the sensitivities of interest through similarity sorting and subsequence matching. Our collaborators were especially intrigued about how quickly similar trends can be resolved with only little user intervention. On the other hand, they clearly stated that the curve plots view alone, without any linkage to a 3D view in which relationships between sensitivities, the shape and location of trajectories, and surrounding atmospheric fields can be monitored, is too limited to enable detailed process understanding.

There was common agreement that the linked 3D trajectory view effectively overcomes the aforementioned limitations. In particular, the embedding of multi-parameter visualizations in the form of bands and pie charts were perceived effective for answering Q3 and Q5, since these options enable performing certain analysis tasks exclusively in the 3D view and can, thus, avoid frequent attention shifts between the curve plots and 3D views.

To study the relative effectiveness of band- and pie chart-based multi-parameter visualization, we have further investigated the impacts of these design choices on identifying certain multi-parameter patterns and comparing them across trajectories. We conducted a task-oriented user study to measure the performance and effectiveness of each mapping, by varying the sensitivity values, the surrounding spatial context and the viewing parameters.

### 5.1 Tasks

We choose the following three representative tasks for the user study, to measure and compare the validity of the different visual designs:

- T1 Finding on which trajectories sensitivities behave against the trend at the current time point.
- T2 Comparing the distributions of sensitivities to a given target distribution.
- T3 Finding groups of trajectories with similar multiparameter distributions.

The study was browser-based to ensure remote participation under the same settings, i.e., participants did not need to install and run Met.3D. Participants were presented images showing either the oriented bands or pie charts,

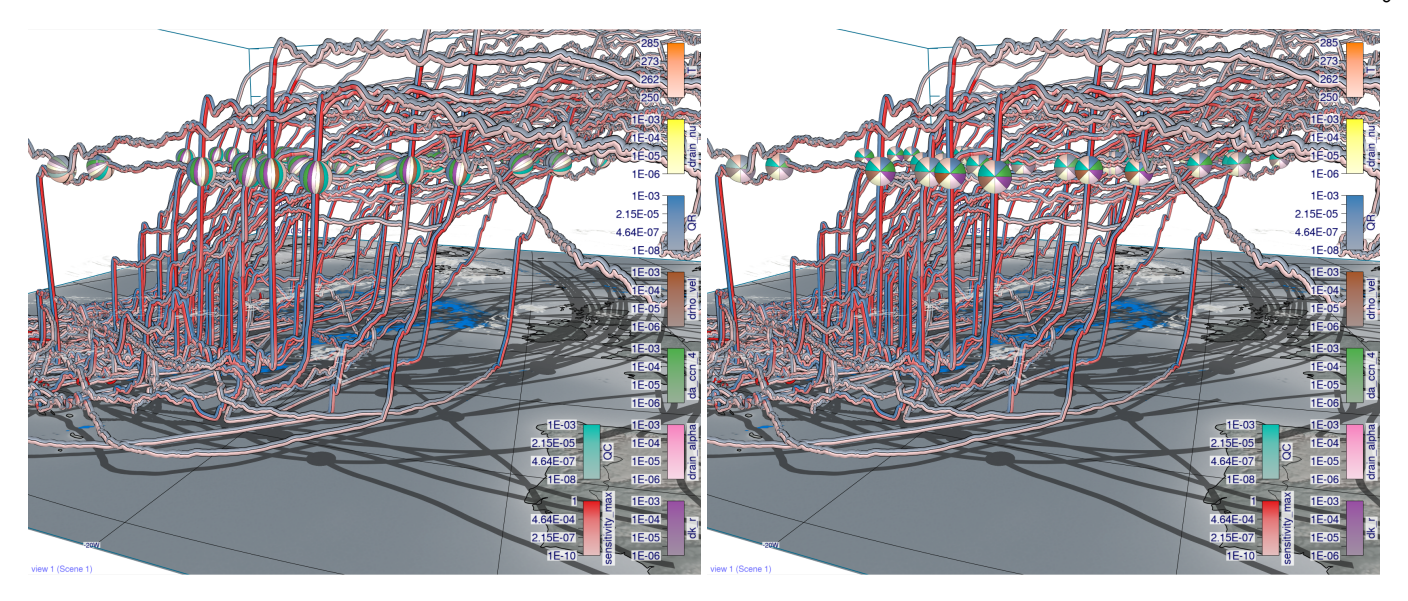


Fig. 7. 50 trajectories from the use-case "Vladiana" using trajectory-oriented bands on spheres and view-aligned pie charts. The different orientations of the bands make it difficult to compare the multi-parameter distributions on different trajectories. With pie charts it is unambiguous which variable is shown, independently of the trajectory orientation.

similar to the images shown in Fig. 7 c) and d). In total, there were 12 design-specific questions, 4 general questions and one free text feedback form. The general questions were regarding the experience of the participant in the fields of meteorology and visualization, and their subjective preference of the two designs.

We recruited 27 participants. 5 (18.5%) stated that they had (experienced) knowledge in 3D visualization, but less or no knowledge in multi-parameter visualization and meteorology. 3 (11.1%) came from the field of meteorology, but were rather un-experienced in 3D and multi-parameter visualization. 5 (18.5%) considered themselves as knowledgeable both in the fields of visualization and meteorology. Participants were first briefed about the study and provided information about the problem, the data, and the visual designs.

### 5.2 Procedure

In the final study, the participants were asked to perform the tasks T1, T2, and T2 in the following ways:

- M1 Participants were asked to select those trajectories where the shown multi-parameter distributions seem to be outliers (at most 25% outliers were shown).
- M2 Participants were asked to select those trajectories where the distribution of all shown quantities is similar to a selected trajectory or a reference distribution.
- M3 Participants were asked to group trajectories based on the shown multi-parameter distributions.

#### 5.3 Analysis

For all tasks, we measured the time it took the users to perform the task, and how accurately the task could be performed. Fig. 8 shows the accumulated results over all participants. Participants were able to answer the questions in 48.1s (bands) and 42.8s (pie charts). A Student's t-test yields a t-value of 1.83 and a p-value of 6.84%, hinting

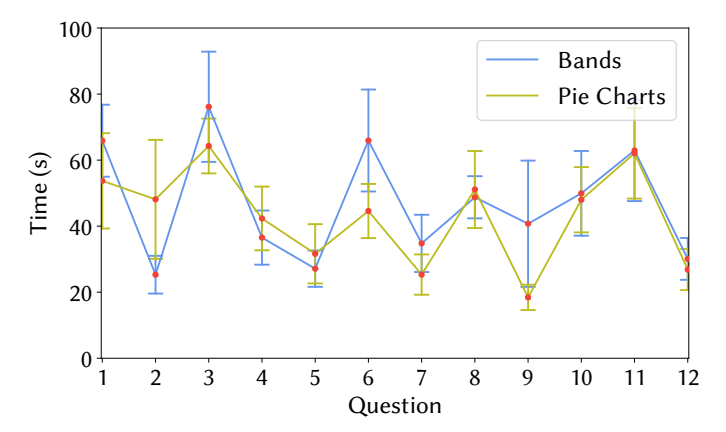


Fig. 8. Average and confidence interval of time participants needed to answer questions in the user study using bands and pie chart-based spheres.

at statistical significance of the deviation between the two distributions. Participants were able to answer the questions correctly with an accuracy of 79.0% (bands) and 79.6% (pie charts). Applying a Student's t-test to this data yields a t-value of -0.138 and a p-value of 89.1%. Thus, we can conclude that there was no statistically significant difference in the accuracy of the participants to solve the tasks between pie charts and bands, however, it is statistically significant that participants could solve the tasks more quickly with the pie charts. About two thirds of the participants stated in the general questions that they preferred the pie charts over the bands-based spheres, while users in the remaining third commended the lens-like character of the bands on the spheres in the free text feedback. Consequently, we believe it should be left up to the users to choose the visual mapping of their choice, with the default being the pie charts.

Since many time steps are shown along the bands, while only one single time step is shown on a pie chart, it was conjectured that peaks could be overlooked in an animation when using pie charts while they remain visible for a longer time when using bands. Multiple users asked for a mouse hover-over to inspect the values of the quantities below the mouse cursor. This feature is already supported, but could not be provided during the image-based study. Two users asked for discrete, quantized color maps instead of the continuous color maps we used in the study. This feature is also already available in Met.3D, and we show an image using quantized 8-class single hue color maps in Appendix G.

Another issue that was raised is the number of different sensitivities that can be well distinguished. In particular, multiple user said that no more than 4-6 different sensitivities should be shown simultaneously, in particular because bands and pie pieces become too small when viewed from a distance. Furthermore, due to decreasing sensitivity with decreasing value, low values were perceived similarly. However, this was not seen as a limitation, because attention is put on the high sensitivity values. What was perceived as problematic by many participants is the number of trajectories that are simultaneously displayed, as comparing the corresponding multi-parameter distributions then becomes tedious. Thus, we support deselecting individual trajectories with the mouse. These trajectories are then desaturated in the 3D view.

### **6** IMPLEMENTATION

All techniques presented in this paper have been integrated into Met.3D, which uses the OpenGL API for GPU-based rendering. For drawing the curve plots view, the vector graphics library NanoVG<sup>2</sup> is embedded. It provides hardware-accelerated rendering of vector graphics elements like anti-aliased lines and polygons, and the specification of scissor geometry to restrict rendering to a rectangular screen region. This is necessary for providing a scroll bar for the content of the curve plots view.

Met.3D offers functionality to render three-dimensional trajectories via illuminated polygonal tubes, including the base map showing the earth surface and shadows cast by the trajectories. However, the specific rendering options required by our approach, i.e., showing view-aligned bands on trajectories and spheres, as well as view-aligned pie charts on spheres, are not available. Notably, these options cannot be realized using object-space texture mapping or standard pixel shaders due to the requirement to keep the color patterns fixed in screen space.

A detailed description of our implementation is given in the Appendix. In the following, we outline the basic concepts underlying the implementation, including additional rendering options.

**View-aligned bands** For rendering the trajectories, it needs to be determined for each fragment that is rendered for the tube surface to which of the n bands in screen space it belongs. Each fragment lies on a circular arc orthogonal to the trajectory tangent (cf. Fig. 9 top). The bands run perpendicular to this arc along the trajectory's tangent direction. In order for the bands to have equal thickness, the angle along the arc to the fragment position is projected onto a line perpendicular to the tangent, which removes the curvature of the arc from the individual bands. The projected arc is

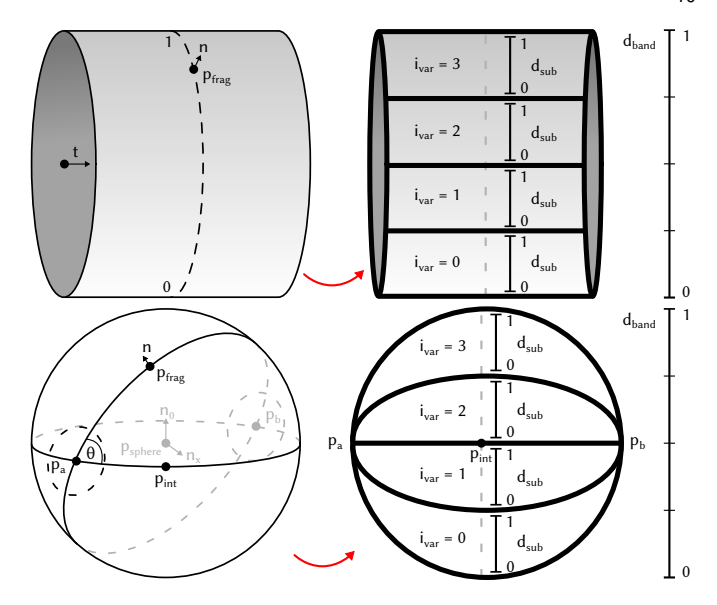


Fig. 9. Top: Illustration of local surface properties and subdivision of the visible part of a trajectory to determine a fragments band position  $d_{band}$ , the sub-band position  $d_{sub}$  and its corresponding variable ID  $i_{var}.$  Bottom: Same as top, but now to compute the band information on a sphere.

then subdivided into n sectors which all have the same height in screen space, and the fragment is classified according to the sectors by computing its relative position  $d_{band}$  in the projection and assigning the corresponding variable index  $i_{var}$  to it. All required parameters can be derived solely from local properties of the rendered surface, i.e., the surface normal vector n, the trajectory tangent vector t and the camera view vector t. In particular, by projecting the camera view direction into the plane orthogonal to the trajectory's tangent direction, the problem of computing the circular arc and the angle it subtends can be reduced to a two-dimensional problem (cf. Fig. 2 in Appendix A).

Bands on a sphere are generated by first rendering each sphere as a polygon model on the GPU. In a preprocess the first  $(p_a)$  and last  $(p_b)$  intersection points between the trajectories and the spheres are computed, including the times  $t_a$  and  $t_b$  at which these intersections occur.  $p_a$  and  $p_b$  are then used in the pixel shader to determine the trajectory direction, and  $t_a$  and  $t_b$  are used to interpolate the parameters continuously along the bands travelling across the surface. The mapping is obtained by first computing the projection of the sphere center  $p_{sphere}$  onto the sphere under the used camera transformation, i.e.  $p_{int}$  (cf. Fig. 9 bottom). The circle going through this point and the points  $p_a$  and  $p_b$ serves as a reference circle relative to which the bands are arranged. Therefore, the normals of the disks  $P_0$  spanned by  $p_a, p_b, p_{int}$  and  $P_{frag}$  spanned by  $p_a, p_b, p_{frag}$  are computed. These two disks meet under a certain angle  $\theta$ . By using this angle and the disks' normals, a measure of the distance to the border of the sphere in screen space can be computed, from which the band position and derived sub-band positions are obtained. To continuously map a parameter onto a band, it is assumed that  $t_a$  and  $t_b$  are linearly interpolated along the line from  $p_a$  to  $p_b$ . The time at the point on this line closest to  $p_{frag}$  is used as the time at  $p_{frag}$ , and the parameter value at this time is read from the trajectory data.

View-aligned pie charts To color a sphere with a pie chart that encodes the values of multiple parameters into its pieces, the screen space projection of the sphere is subdivided into a predefined number of individual pieces. To achieve a consistent assignment of parameters to pieces for all spheres, first the angle  $\alpha_{band}$  representing the angular distance of a fragment  $p_{frag}$  to the up-axis of the camera is computed. The global band position  $d_{band}$  is then given by

$$d_{band} = \frac{\alpha_{band} \bmod 2\pi}{2\pi}.$$
 (2)

When mapping N parameters onto the sphere, the band position  $d_{band} \in [0,1)$  is subdivided into multiple sub-band positions  $d_{sub}$ .

### 7 RESULTS: CASE-STUDY "VLADIANA"

We demonstrate the value of our method by discussing first investigations of the sensitivity of the rain mass density (QR) simulated by the NWP model to microphysical parameters along WCB trajectories within cyclone "Vladiana". We are particularly interested in whether there are differences in the sensitivities along the ascent based on the location and the ascent rate. For this analysis, we first employed the exploratory visual analysis capabilities of the proposed method to identify the regions and times of interest. Appendix E demonstrates how the domain scientists selected the trajectories of interest. In this section, we will focus on these specific selected trajectories to analyze the joint development of multiple sensitivity parameters. WCB trajectories ascend in a wide region near the extratropical cyclones' fronts between 23 September 2016 and 26 September 2016. For the example presented here, we compare sensitivities related to QR along trajectories in different regions of the cyclone. From a total of 8744 available WCB trajectories we select two groups of trajectories, one in the north and one in the south of the region of interest (cf. Fig. 10). From both groups, we select ten trajectories each, those five with the slowest ascent and those five with the fastest ascent. This results in 20 trajectories with a large variance in their ascent rate and location.

Fig. 11 shows curve plots with trajectories selected either from the southern (Fig. 11a) or northern (Fig. 11b) group, to analyze trends of parameters across one or more groups of trajectories (Q1, Q2, and Q3). We select QR as target variable, and center the x-axis by the time of rapid ascent of each trajectory. The different locations of peaks in QR for both groups stand out. The southern group has QR maxima at the start of the ascent, while the northern group has larger QR maxima a few hours before the ascent starts. Such high QR along trajectories can arise from either (i) sedimentation of rain from above (influenced by parameters alpha, beta, and gamma in the numerical model's parameterization) or (ii) local production from collision of available cloud droplets (influenced by the cloud condensation nuclei (CCN), the mass density of cloud droplets (QC), and a cloud collision parameter (k\_r); for detailed description of these parameters see [10], [60]). Hence, we are interested in which process dominates in which region. The automated ordering (Subsec. 4.1) of the parameters provides further insight. The parameters are sorted by similarity in each

time step to the maximum of QR. The sensitivities to the parameters rain\_alpha, rain\_beta, rain\_gamma (used for sedimentation velocity), and rain\_nu (used in the particlemass distribution of rain droplets) are the variables with the highest similarity to QR in both cases.

Sensitivities to CCN parameters and to k\_r are ranked higher in the southern group, indicating that rain droplets' formation due to collisions of cloud droplets are closely related to local QR formation. These correlations are not present in the northern group, which indicates that local QR maxima result from sedimentation of precipitation from above. We conclude that rain formation, specifically local maxima of QR, in the southern group is more closely related to the formation of cloud droplets and, therefore, the updraft w of the trajectories than in the northern group (Q3).

To elaborate on Q3, we compare the maximum sensitivity of QR to any parameter in Fig. 10. The blue color along trajectories shows QR, whereas red indicates the maximum sensitivity to any parameter. Low sensitivity values (i.e., unsaturated bands) appear mostly when the trajectories descend and after they have reached their maximum height (Fig. 10a,b). This emphasizes that processes influencing QR dominate at lower altitude and during updrafts.

The curve plots in Fig. 11 are centered at the start of the ascent to address Q4. The variance of the sensitivities (blue shades) is similarly distributed for both groups, but peaks appear at different times. We can infer that the variance between trajectories with different locations of ascent is higher than between trajectories with a similar location.

At last, we investigate differences in sensitivities between convective and slantwise trajectories (Q5). We synchronize the height of the spheres along trajectories and select three variables (QC, QR, and temperature) and model parameters with a high ranking from Fig. 11. The color intensities of da\_ccn\_4 (green) in slantwise ascending trajectories (e.g., Fig. 10a) is lower than for convective ones. This indicates that processes associated with a\_ccn\_4 have a smaller effect on QR during slantwise ascent. Furthermore, the collision of cloud droplets (dk\_r; purple color) is more important during convective ascent. This agrees with our previous assessment, and shows that the formation of cloud droplets and their subsequent conversion to QR are more important for convective ascent than for slantwise ascent.

For a more detailed analysis, we zoom in to one slantwise ascending trajectory, and use multiple bands to show each parameter (cf. Fig. 12). Fig. 12 reveals an alternating pattern between dk\_r (purple) and da\_ccn\_4 (green). The overall slantwise ascent of the trajectory shows short periods of sharp ascent with strong cloud droplet formation. These periods are interrupted by periods of slower ascent, where the collision of cloud droplets dominates. These processes do not alternate in convectively ascending trajectories (cf. Fig. 13) and rather occur simultaneously. This can produce and accumulate large amounts of QR quickly, cf. Fig. 10c with slantwise trajectories in the background and convective trajectories in the foreground, leading to more intense surface precipitation in a limited area. In contrast, slantwise ascent spreads these processes over a larger area, explaining the impact of such trajectories on large-scale precipitation patterns [5], [6], [7], [70].

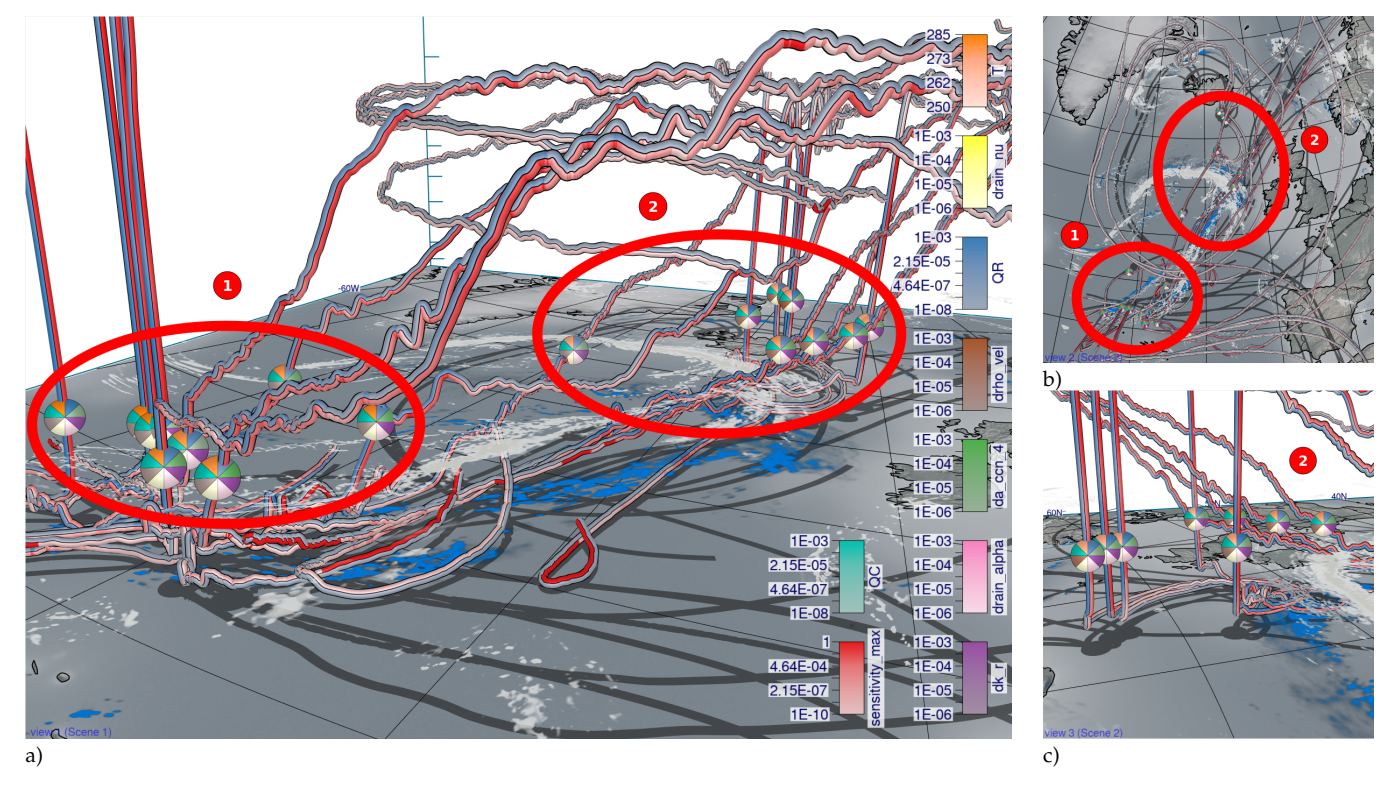


Fig. 10. Overview of selected trajectories and first insights with spheres at the same height. Low-level clouds at approximately 1500 m altitude (gray) and surface precipitation (blue) are shown at 07 UTC 23 September 2016 when multiple trajectories start their ascent. a) Trajectories ascending in the south (group 1) and in the north (group 2) with spheres showing eight variables each. b) View from the top with the northern group 2 near clouds and precipitation and the southern group 1 with less clouds and precipitation. c) A close-up view of group 2.

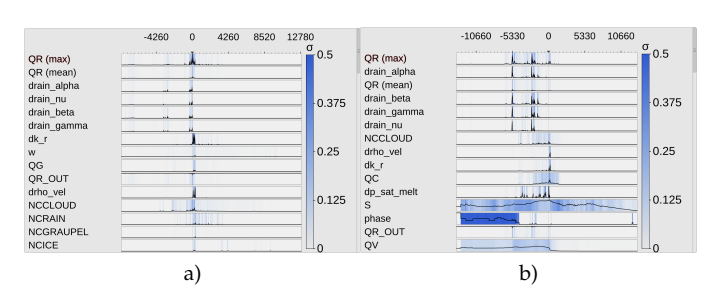


Fig. 11. The curve plots are centered at the start of the ascent of the trajectories. The labels for the x-axis show the simulation time step, where each simulation step stands for 20 s. a) Only trajectories from the southern group have been selected. There are large peaks for rain mass density (QR) around the start of the ascent, indicating precipitation from above. b) Trajectories from the northern group with a peak in QR several hours before their ascent starts.

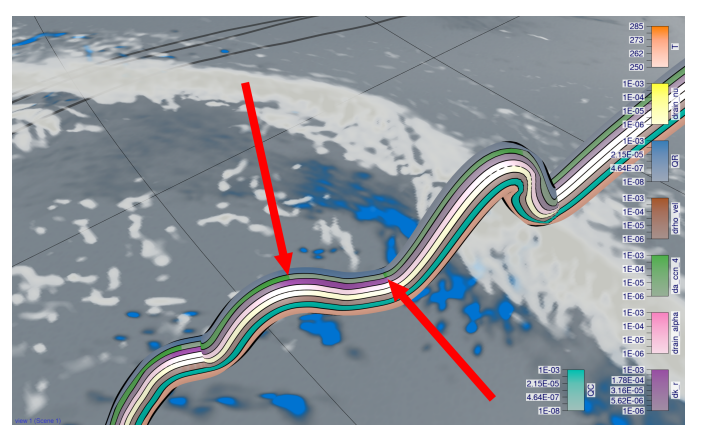


Fig. 12. Zoomed in at a slantwise trajectory. The green band (da\_ccn\_4 associated with cloud droplet formation) alternates with the purple band (dk\_r associated with cloud droplet collision to form raindrops).

### 8 CONCLUSION AND FUTURE WORK

We propose a novel visual analysis workflow to investigate the relationships between the sensitivity of a target variable to changes in model parameters and the location and shape of WCB trajectories. This information is required to analyze the validity of physical assumptions on which microphysical parameterizations in the numerical model codes are based. Making the sensitivities accessible along important features such as WCB trajectories offers new insights into the correlation structures between different parameters and differences between trajectories. To perform these analyses in an effective way, we link a curve plot-based summary view with a novel sphere-based focus view

that enables comparison of multi-parameter distributions on different trajectories. The curve plots view provides statistical overviews and enables to quickly find parameters with similar temporal evolution. We develop the workflow in a team of scientists from visualization, high-performance computing and meteorology, and integrate it into the open-source meteorological visualization software Met.3D. The usability and benefits of the workflow is demonstrated with a real-world case-study.

In the future, we intend to extend the workflow in multiple ways. Firstly, we will investigate how to effectively show additional 3D atmospheric fields, or features in these fields,

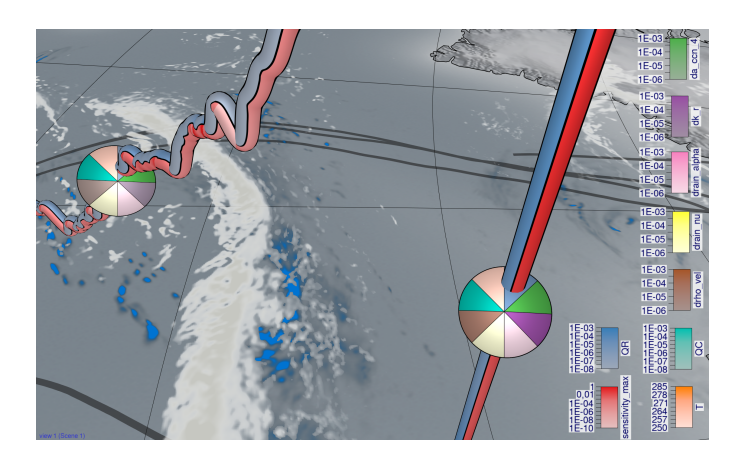


Fig. 13. Zoomed in at a convective trajectory with the slantwise trajectory from Fig. 12 on the left. The green (da\_ccn\_4 associated with cloud droplet formation) and purple sensitivity (dk\_r associated with cloud droplet collision to form raindrops) have simultaneously high values during the convective ascent.

in the surrounding of trajectories, to reveal specific regional multi-field patterns causing high sensitivities. Secondly, we intend to make the workflow usable with ensembles of trajectories, where multiple sets of trajectories from different simulation runs are considered. In this way, relationships between sensitivities and the ensemble spread can be examined. Thirdly, we are going to support multiple target variables that can be switched interactively. Furthermore, the atmospheric scientists are currently analyzing parameter sensitivities in another WCB case-study simulated with the state-of-the-art NWP model ICON [71]. The visualization and analysis framework presented here will also be applied for the systematic analysis and mapping of sensitivities in this follow-up case-study.

### **ACKNOWLEDGMENTS**

The authors acknowledge support by the Deutsche Forschungsgemeinschaft (DFG) within the Transregional Collaborative Research Centre TRR165 Waves to Weather, (www.wavestoweather.de), Projects A7, Z2 and B8 as well as funding from JGU Mainz.

### REFERENCES

- H. Wernli, "A lagrangian-based analysis of extratropical cyclones. II: A detailed case-study," Q. J. R. Meteorol. Soc., vol. 123, no. 542, pp. 1677–1706, 1997.
- [2] E. Madonna, H. Wernli, H. Joos, and O. Martius, "Warm conveyor belts in the ERA-interim dataset (1979–2010). part i: Climatology and potential vorticity evolution," J. Clim., vol. 27, no. 1, pp. 3–26, 2014.
- [3] D. Büeler and S. Pfahl, "Potential vorticity diagnostics to quantify effects of latent heating in extratropical cyclones. part i: Methodology," J. Atmos. Sci., vol. 74, no. 11, pp. 3567–3590, 2017.
- [4] S. Pfahl, E. Madonna, M. Boettcher, H. Joos, and H. Wernli, "Warm conveyor belts in the ERA-interim dataset (1979–2010). part II: Moisture origin and relevance for precipitation," vol. 27, no. 1, pp. 27–40, 2014.
- [5] A. Oertel, M. Boettcher, H. Joos, M. Sprenger, and H. Wernli, "Potential vorticity structure of embedded convection in a warm conveyor belt and its relevance for large-scale dynamics," Weather Clim. Dynam., vol. 1, no. 1, pp. 127–153, 2020.

- [6] A. Oertel, M. Sprenger, H. Joos, M. Boettcher, H. Konow, M. Hagen, and H. Wernli, "Observations and simulation of intense convection embedded in a warm conveyor belt how ambient vertical wind shear determines the dynamical impact," Weather Clim. Dynam., vol. 2, no. 1, pp. 89–110, 2021.
- [7] J. Jeyaratnam, J. F. Booth, C. M. Naud, Z. J. Luo, and C. R. Homeyer, "Upright convection in extratropical cyclones: A survey using ground-based radar data over the united states," *Geophysical Research Letters*, vol. 47, no. 4, 2020.
- [8] A. Griewank and A. Walther, Evaluating Derivatives: Principles and Techniques of Algorithmic Differentiation, Second Edition. SIAM, 2008
- [9] M. Baumgartner, M. Sagebaum, N. R. Gauger, P. Spichtinger, and A. Brinkmann, "Algorithmic differentiation for cloud schemes (IFS cy43r3) using CoDiPack (v1.8.1)," *Geosci. Model Dev.*, vol. 12, no. 12, pp. 5197–5212, 2019.
- [10] M. Hieronymus, M. Baumgartner, A. Miltenberger, and A. Brinkmann, "Algorithmic Differentiation for Sensitivity Analysis in Cloud Microphysics," *Journal of Advances in Modeling Earth* Systems, Jun. 2022.
- [11] A. K. Miltenberger, S. Pfahl, and H. Wernli, "An online trajectory module (version 1.0) for the nonhydrostatic numerical weather prediction model COSMO," *Geosci. Model Dev.*, vol. 6, no. 6, pp. 1989–2004, 2013.
- [12] S. Raveh-Rubin, "Dry intrusions: Lagrangian climatology and dynamical impact on the planetary boundary layer," *Journal of Climate*, vol. 30, no. 17, pp. 6661 – 6682, 2017.
- [13] M. Rautenhaus, M. Kern, A. Schäfler, and R. Westermann, "Three-dimensional visualization of ensemble weather forecasts part 1: The visualization tool met.3d (version 1.0)," Geoscientific Model Development, vol. 8, no. 7, p. 2329–2353, 2015.
- [14] A. L. Love, A. Pang, and D. L. Kao, "Visualizing spatial multivalue data," *IEEE Computer Graphics and Applications*, vol. 25, no. 3, pp. 69–79, 2005.
- [15] K. Potter, J. Kniss, R. Riesenfeld, and C. R. Johnson, "Visualizing summary statistics and uncertainty," Computer Graphics Forum, vol. 29, no. 3, pp. 823–832, 2010.
- [16] J. Wang, S. Hazarika, C. Li, and H. Shen, "Visualization and visual analysis of ensemble data: A survey," *IEEE Transactions on Visualization and Computer Graphics*, pp. 1–1, 2018.
- [17] A. T. Pang, C. M. Wittenbrink, and S. K. Lodha, "Approaches to uncertainty visualization," *The Visual Computer*, vol. 13, no. 8, pp. 370–390, 1997.
- [18] R. T. Whitaker, M. Mirzargar, and R. M. Kirby, "Contour boxplots: A method for characterizing uncertainty in feature sets from simulation ensembles," *IEEE Transactions on Visualization and Computer Graphics*, vol. 19, no. 12, pp. 2713–2722, Dec 2013.
- [19] F. Ferstl, M. Kanzler, M. Rautenhaus, and R. Westermann, "Visual analysis of spatial variability and global correlations in ensembles of Iso-Contours," *Computer Graphics Forum*, vol. 35, no. 3, pp. 221– 230, 2016.
- [20] D. Thompson, J. A. Levine, J. C. Bennett, P.-T. Bremer, A. Gyulassy, V. Pascucci, and P. P. Pébay, "Analysis of large-scale scalar data using hixels," in 2011 IEEE Symposium on Large Data Analysis and Visualization. IEEE, 2011, pp. 23–30.
- [21] I. Demir, C. Dick, and R. Westermann, "Multi-charts for comparative 3d ensemble visualization," *IEEE Transactions on Visualization and Computer Graphics*, vol. 20, no. 12, Dec. 2014.
- [22] S. Liu, J. A. Levine, P.-T. Bremer, and V. Pascucci, "Gaussian mixture model based volume visualization," in *IEEE Symposium* on Large Data Analysis and Visualization (LDAV). IEEE, 2012, pp. 73–77.
- [23] M. Jarema, I. Demir, J. Kehrer, and R. Westermann, "Comparative visual analysis of vector field ensembles," in *IEEE Conference on Visual Analytics Science and Technology (VAST)*, 2015, pp. 81–88.
- [24] S. Dutta and H.-W. Shen, "Distribution driven extraction and tracking of features for time-varying data analysis," *IEEE Trans*actions on Visualization and Computer Graphics, vol. 22, no. 1, pp. 837–846, 2015.
- [25] K.-C. Wang, K. Lu, T.-H. Wei, N. Shareef, and H.-W. Shen, "Statistical visualization and analysis of large data using a value-based spatial distribution," in 2017 IEEE Pacific Visualization Symposium (Pacific Vis.). IEEE, 2017, pp. 161–170.
- [26] S. Hazarika, A. Biswas, and H.-W. Shen, "Uncertainty visualization using copula-based analysis in mixed distribution models," IEEE Transactions on Visualization and Computer Graphics, vol. 24, no. 1, pp. 934–943, 2017.

- [27] C. Tominski, H. Schumann, G. Andrienko, and N. Andrienko, "Stacking-based visualization of trajectory attribute data," *IEEE Transactions on Visualization and Computer Graphics*, vol. 18, no. 12, pp. 2565–2574, 2012.
- [28] R. Scheepens, N. Willems, H. van de Wetering, G. Andrienko, N. Andrienko, and J. J. van Wijk, "Composite density maps for multivariate trajectories," *IEEE Transactions on Visualization and Computer Graphics*, vol. 17, no. 12, pp. 2518–2527, 2011.
- [29] K. Bürger, R. Fraedrich, D. Merhof, and R. Westermann, "Instant visitation maps for interactive visualization of uncertain particle trajectories," in *Visualization and Data Analysis* 2012, P. C. Wong, D. L. Kao, M. C. Hao, C. Chen, R. Kosara, M. A. Livingston, J. Park, and I. Roberts, Eds., vol. 8294, International Society for Optics and Photonics. SPIE, 2012, p. 82940P.
- [30] J. L. Hintze and R. D. Nelson, "Violin plots: A box plot-density trace synergism," *The American Statistician*, vol. 52, no. 2, pp. 181– 184, 1998.
- [31] T. Höllt, A. Magdy, G. Chen, G. Gopalakrishnan, I. Hoteit, C. D. Hansen, and M. Hadwiger, "Visual analysis of uncertainties in ocean forecasts for planning and operation of off-shore structures," in 2013 IEEE Pacific Visualization Symposium (PacificVis), Feb 2013, pp. 185–192.
- [32] W. He, J. Wang, H. Guo, H.-W. Shen, and T. Peterka, "Cecav-dnn: Collective ensemble comparison and visualization using deep neural networks," Visual Informatics, 2020.
- [33] A. Kumpf, J. Stumpfegger, P. F. Härtl, and R. Westermann, "Visual analysis of multi-parameter distributions across ensembles of 3d fields," *IEEE Transactions on Visualization and Computer Graphics*, pp. 1–1, 2021.
- [34] A. Inselberg, "The plane with parallel coordinates," *The visual computer*, vol. 1, no. 2, pp. 69–91, 1985.
- [35] A. Inselberg and B. Dimsdale, "Parallel coordinates," in Human-Machine Interactive Systems. Springer, 1991, pp. 199–233.
- [36] J. Heinrich and D. Weiskopf, "State of the art of parallel coordinates." in *Eurographics (STARs)*, 2013, pp. 95–116.
- [37] S. Bruckner and T. Moller, "Result-driven exploration of simulation parameter spaces for visual effects design," *IEEE Transactions* on Visualization and Computer Graphics, vol. 16, no. 6, pp. 1468–1476, 2010.
- [38] S. Bergner, M. Sedlmair, T. Moller, S. N. Abdolyousefi, and A. Saad, "Paraglide: Interactive parameter space partitioning for computer simulations," *IEEE Transactions on Visualization and Computer Graphics*, vol. 19, no. 9, pp. 1499–1512, 2013.
- [39] T. Torsney-Weir, A. Saad, T. Möller, H.-C. Hege, B. Weber, J.-M. Verbavatz, and S. Bergner, "Tuner: Principled parameter finding for image segmentation algorithms using visual response surface exploration," *IEEE Transactions on Visualization and Computer Graphics*, vol. 17, no. 12, pp. 1892–1901, 2011.
- [40] M. Sedlmair, C. Heinzl, S. Bruckner, H. Piringer, and T. Möller, "Visual parameter space analysis: A conceptual framework," *IEEE Transactions on Visualization and Computer Graphics*, vol. 20, no. 12, pp. 2161–2170, Dec 2014.
- [41] F. Sadlo, R. Peikert, and M. Sick, "Visualization tools for vorticity transport analysis in incompressible flow," *IEEE Transactions on Visualization and Computer Graphics*, vol. 12, no. 5, pp. 949–956, 2006
- [42] M. Rautenhaus, M. Böttinger, S. Siemen, R. Hoffman, R. M. Kirby, M. Mirzargar, N. R'ober, and R. Westermann, "Visualization in meteorology - a survey of techniques and tools for data analysis tasks," *IEEE Transactions on Visualization and Computer Graphics*, vol. PP, no. 99, 2017.
- [43] S. Afzal, M. Hittawe, S. Ghani, T. Jamil, O. Knio, M. Hadwiger, and I. Hoteit, "The state of the art in visual analysis approaches for ocean and atmospheric datasets," *Computer Graphics Forum*, vol. 38, no. 3, pp. 881–907, 2019.
- [44] A. Yoshizumi, M. M. Coffer, E. L. Collins, M. D. Gaines, X. Gao, K. Jones, I. R. McGregor, K. A. McQuillan, V. Perin, L. M. Tomkins, T. Worm, and L. Tateosian, "A review of geospatial content in ieee visualization publications," in 2020 IEEE Visualization Conference (VIS), 2020, pp. 51–55.
- [45] L. Orf, R. Wilhelmson, B. Lee, C. Finley, and A. Houston, "Evolution of a Long-Track Violent Tornado within a Simulated Supercell," Bull. Amer. Meteor. Soc., May 2016.
- [46] M. Meyer, I. Polkova, K. R. Modali, L. Schaffer, J. Baehr, S. Olbrich, and M. Rautenhaus, "Interactive 3-D visual analysis of ERA5 data: Improving diagnostic indices for marine cold air outbreaks and

- polar lows," Weather and Climate Dynamics, vol. 2, no. 3, pp. 867–891, Sep. 2021.
- [47] W. Engelke, T. B. Masood, J. Beran, R. Caballero, and I. Hotz, "Topology-Based Feature Design and Tracking for Multi-center Cyclones," in *Topological Methods in Data Analysis and Visualization* VI, I. Hotz, T. Bin Masood, F. Sadlo, and J. Tierny, Eds. Cham: Springer International Publishing, 2021, pp. 71–85.
- [48] C. Kappe, M. Böttinger, and H. Leitte, "Topology-based feature analysis of scalar field ensembles: An application to climate (change) analysis," *Computers & Graphics*, 2022.
- [49] R. Bader, M. Sprenger, N. Ban, S. Radisuhli, C. Schar, and T. Günther, "Extraction and Visual Analysis of Potential Vorticity Banners around the Alps," *IEEE Transactions on Visualization and Computer Graphics*, pp. 1–1, 2019.
- [50] L. Bösiger, M. Sprenger, M. Boettcher, H. Joos, and T. Günther, "Integration-based extraction and visualization of jet stream cores," *Geoscientific Model Development*, vol. 15, no. 3, pp. 1079– 1096, 2022.
- [51] M. Kern, T. Hewson, F. Sadlo, R. Westermann, and M. Rautenhaus, "Robust detection and visualization of jet-stream core lines in atmospheric flow," *IEEE Transactions on Visualization and Computer Graphics*, vol. 24, no. 1, pp. 893–902, 2018.
- [52] M. Kern, T. Hewson, A. Schatler, R. Westermann, and M. Rautenhaus, "Interactive 3D Visual Analysis of Atmospheric Fronts," *IEEE Transactions on Visualization and Computer Graphics*, vol. 25, no. 1, pp. 1080–1090, Jan. 2019.
- [53] M. Rautenhaus, C. M. Grams, A. Schäfler, and R. Westermann, "Three-dimensional visualization of ensemble weather forecasts – Part 2: Forecasting warm conveyor belt situations for aircraft-based field campaigns," *Geosci. Model Dev.*, vol. 8, no. 7, pp. 2355–2377, 2015.
- [54] C. H. Bischof, G. D. Pusch, and R. Knoesel, "Sensitivity analysis of the MM5 weather model using automatic differentiation," *Comput. Phys.*, vol. 10, no. 6, p. 605, 1996.
- [55] A. Paszke, S. Gross, F. Massa, A. Lerer, J. Bradbury, G. Chanan, T. Killeen, Z. Lin, N. Gimelshein, L. Antiga, A. Desmaison, A. Kopf, E. Yang, Z. DeVito, M. Raison, A. Tejani, S. Chilamkurthy, B. Steiner, L. Fang, J. Bai, and S. Chintala, "PyTorch: An imperative style, high-performance deep learning library," in *Advances in Neural Information Processing Systems* 32, H. Wallach, H. Larochelle, A. Beygelzimer, F. d. Alché-Buc, E. Fox, and R. Garnett, Eds. Curran Associates, Inc., 2019, pp. 8024–8035.
- [56] C. C. Margossian, "A review of automatic differentiation and its efficient implementation," WIREs Data Min. Knowl. Discov., vol. 9, no. 4, 2019.
- [57] T. A. Albring, M. Sagebaum, and N. R. Gauger, Development of a Consistent Discrete Adjoint Solver in an Evolving Aerodynamic Design Framework, 2015.
- [58] A. Schäfler, G. Craig, H. Wernli, P. Arbogast, J. D. Doyle, R. McTaggart-Cowan, J. Methven, G. Rivière, F. Ament, M. Boettcher, M. Bramberger, Q. Cazenave, R. Cotton, S. Crewell, J. Delanoë, A. Dörnbrack, A. Ehrlich, F. Ewald, A. Fix, C. M. Grams, S. L. Gray, H. Grob, S. Groß, M. Hagen, B. Harvey, L. Hirsch, M. Jacob, T. Kölling, H. Konow, C. Lemmerz, O. Lux, L. Magnusson, B. Mayer, M. Mech, R. Moore, J. Pelon, J. Quinting, S. Rahm, M. Rapp, M. Rautenhaus, O. Reitebuch, C. A. Reynolds, H. Sodemann, T. Spengler, G. Vaughan, M. Wendisch, M. Wirth, B. Witschas, K. Wolf, and T. Zinner, "The north atlantic waveguide and downstream impact experiment," Bull. Amer. Meteor. Soc., vol. 99, no. 8, pp. 1607–1637, 2018.
- [59] M. Baldauf, A. Seifert, J. Förstner, D. Majewski, M. Raschendorfer, and T. Reinhardt, "Operational convective-scale numerical weather prediction with the COSMO model: Description and sensitivities," Mon. Weather Rev., vol. 139, no. 12, pp. 3887–3905, 2011.
- [60] A. Seifert and K. D. Beheng, "A two-moment cloud microphysics parameterization for mixed-phase clouds. part 1: Model description," *Meteorol. Atmos. Phys.*, vol. 92, no. 1, pp. 45–66, 2006.
- [61] B. Kärcher, J. Hendricks, and U. Lohmann, "Physically based parameterization of cirrus cloud formation for use in global atmospheric models," J. Geophys. Res. Atmos., vol. 111, p. D01205, 2006.
- [62] V. T. J. Phillips, P. J. DeMott, and C. Andronache, "An empirical parameterization of heterogeneous ice nucleation for multiple chemical species of aerosol," *J. Atmos. Sci.*, vol. 65, no. 9, pp. 2757– 2783, 2008.

- [63] M. Sagebaum, T. Albring, and N. R. Gauger, "High-performance derivative computations using CoDiPack," ACM Trans. Math. Softw., vol. 45, no. 4, pp. 1–26, 2019.
- [64] S. Steinarsson, "Downsampling time series for visual representation," Master's thesis, University of Iceland, 2013. [65] M. Toyoda and Y. Sakurai, "Subsequence matching in data
- streams," NTT Technical Review, vol. 11, no. 1, pp. 208–208, 2013.
- [66] L. Chen, M. T. Özsu, and V. Oria, "Robust and fast similarity search for moving object trajectories," in *Proceedings of the 2005* ACM SIGMOD International Conference on Management of Data, ser. SIGMOD '05. New York, NY, USA: Association for Computing Machinery, 2005, p. 491-502.
- [67] Y. Sakurai, C. Faloutsos, and M. Yamamuro, "Stream monitoring under the time warping distance," in 2007 IEEE 23rd International Conference on Data Engineering, 2007, pp. 1046–1055.
  [68] X. Gong, Y.-W. Si, S. Fong, and S. Mohammed, "Nspring:
- Normalization-supported spring for subsequence matching on time series streams," in 2014 IEEE 15th International Symposium on Computational Intelligence and Informatics (CINTI), 2014, pp. 373-
- [69] M. Harrower and C. A. Brewer, "Colorbrewer.org: An online tool for selecting colour schemes for maps," The Cartographic Journal, vol. 40, no. 1, pp. 27–37, 2003.
- [70] A. Oertel, M. Boettcher, H. Joos, M. Sprenger, H. Konow, M. Hagen, and H. Wernli, "Convective activity in an extratropical cyclone and its warm conveyor belt - a case-study combining observations and a convection-permitting model simulation," Q. J. R. Meteorol. Soc., vol. 145, no. 721, pp. 1406–1426, 2019.
- [71] G. Zängl, D. Reinert, P. Rípodas, and M. Baldauf, "The ICON (ICOsahedral Non-hydrostatic) modelling framework of DWD and MPI-M: Description of the non-hydrostatic dynamical core," Quarterly Journal of the Royal Meteorological Society, vol. 141, no. 563–579, pp. 563–579, 2015.



Christoph Neuhauser is a PhD candidate at the Computer Graphics and Visualization Group at the Technical University of Munich (TUM). He received his Bachelor's and Master's degrees in computer science from TUM in 2019 and 2020. Major interests in research comprise scientific visualization and real-time rendering.



Maicon Hieronymus is a PhD candidate at the Efficient Computing and Storage Group at the Johannes Gutenberg University Mainz (JGU) since 2019. He studied computer science (B.Sc.) and computer science with minor in physics (M.Sc.) at JGU. Research interests involve model analysis of cloud microphysical models and algorithmic differentiation in atmospheric physics.



Michael Kern is a research scientist and software engineer at Advanced Micro Devices (AMD) with major focus on real-time computer graphics and ray tracing. He studied computer science and received his Ph.D. from TUM in 2020. His thesis was concerned about feature detection and uncertainty visualization in meteorological data. Besides work, his main interests are scientific visualization and high-performance GPU computing.



Marc Rautenhaus received the M.Sc. degree in atmospheric science from the University of British Columbia, Vancouver, in 2007, and the Ph.D. degree in computer science from TUM, Munich, in 2015. He currently leads the Visual Data Analysis Group at the Regional Computing Centre of Universität Hamburg. Marc's research interests focus on the intersection of visualization, data analysis, and meteorology.



Annika Oertel Annika Oertel studied atmospheric science and received a Ph.D. in atmospheric dynamics from ETH Zurich. Since 2020 she works as postdoctoral researcher in the Institute of Meteorology and Climate Research at Karlsruhe Institute of Technology. Her research focuses on the model representation of microphysical processes in warm conveyor belts and their interactions with the larger-scale extratropical circulation.



Rüdiger Westermann studied computer science at the Technical University Darmstadt and received his Ph.D. in computer science from the University of Dortmund, both in Germany. In 2002, he was appointed the chair of Computer Graphics and Visualization at TUM. His research interests include scalable data visualization and simulation algorithms, GPU computing, real-time rendering of large data, and uncertainty visual-

### Appendix: Visual Analysis of Multiple Dynamic Sensitivities along Ascending Trajectories in the Atmosphere

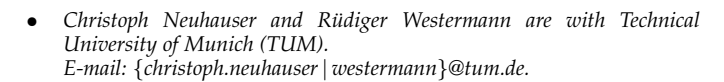
Christoph Neuhauser, Maicon Hieronymus, Michael Kern, Marc Rautenhaus, Annika Oertel, and Rüdiger Westermann

Abstract—Numerical weather prediction models rely on parameterizations for subgrid-scale processes, e.g., for cloud microphysics. These parameterizations are a well-known source of uncertainty in weather forecasts that can be quantified via algorithmic differentiation, which computes the sensitivities of prognostic variables to changes in model parameters. It is particularly interesting to use sensitivities to analyze the validity of physical assumptions on which microphysical parameterizations in the numerical model source code are based. In this article, we consider the use case of strongly ascending trajectories, so-called warm conveyor belt trajectories, known to have a significant impact on intense surface precipitation rates in extratropical cyclones. We present visual analytics solutions to analyze interactively the sensitivities of a selected prognostic variable, i.e. rain mass density, to multiple model parameters along such trajectories. We propose a visual interface that enables to a) compare the values of multiple sensitivities at a single time step on multiple trajectories, b) assess the spatio-temporal relationships between sensitivities and the shape and location of trajectories, and c) a comparative analysis of the temporal development of sensitivities along multiple trajectories. We demonstrate how our approach enables atmospheric scientists to interactively analyze the uncertainty in the microphysical parameterizations, and along the trajectories, with respect to a selected prognostic variable. We apply our approach to the analysis of convective trajectories within the extratropical cyclone "Vladiana", which occurred between 22-25 September 2016 over the North Atlantic.

Index Terms—Meteorology, trajectories, temporal data, multi-parameter data, diagrams, linking, focus+context, sensitivity analysis.

### APPENDIX A TUBE RENDERING

TO obtain a renderable trajectory representation, the trajectory (i.e. 3D pathlines) are polygonized by extruding them into tubes in a GPU geometry shader. The parameters are mapped onto the surface of the tube as a set of bands running in the direction of the trajectory tangent (cf. Fig. 1). When mapping the bands onto the tube in object space, occlusion effects can occur, as not all parameters may lie in the front, visible part of the tube. Also, due to twist and rotations around the tube, the order in which the bands appear on screen can change and make a comparison between different tubes and the association of parameters to bands more difficult. To avoid this, our rendering technique aligns the bands in view space and keeps their relative order on the screen fix, independent of the viewing direction. For this, a screen space band position  $d_{band}$  is computed in the pixel shader on the GPU using only the tangent vector t of



Maicon Hieronymus is with Johannes Gutenberg University Mainz. E-mail: mhieronymus@uni-mainz.de.

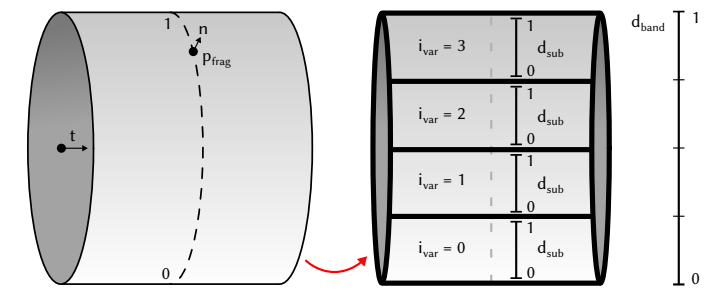


Fig. 1. Illustration of local surface properties and subdivision of the visible part of a trajectory to determine a fragments band position  $d_{band}$ , the sub-band position  $d_{sub}$  and its corresponding variable ID  $i_{var}$ .

the pathline associated with the tube surface fragment, the surface normal n and the view vector  $v = \frac{p_{cam} - p_{frag}}{\|p_{cam} - p_{frag}\|_2}$  pointing from the fragment towards the camera position  $p_{cam}$  as inputs.

By projecting the camera view direction into the plane orthogonal to the tangent direction of the trajectory, the problem of computing the band position can be reduced to a two-dimensional problem. The projected camera direction v' can be computed by using  $v_{aux} = \frac{t \times v}{\|t \times v\|_2}$  as  $v' = \frac{v_{aux} \times t}{\|v_{aux} \times t\|_2}$ . The resulting setting is shown in Fig. 2.

Using the angle  $\phi = \angle(v',n)$  between the projected view vector v' and the normal vector n would unfortunately not be sufficient as a measure, because it does not change linearly in screen space, thus producing bands of differing width. In order to derive the desired screen space

Michael Kern is with Advanced Micro Devices, Inc. E-mail: Michael.Kern@amd.com.

Marc Rautenhaus is with Universität Hamburg. E-mail: marc.rautenhaus@uni-hamburg.de.

Annika Oertel is with Karlsruhe Institute of Technology. E-mail: annika.oertel@kit.edu.

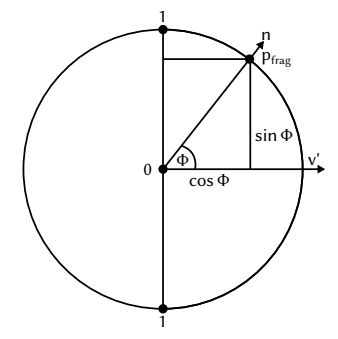


Fig. 2. Cross section of the tube with the plane perpendicular to the tangent vector  $\boldsymbol{t}$  of the pathline.

measure, the fragment position needs to be projected onto an imaginary band, illustrated as the vertical line in Fig. 2. As can be seen in the figure, the normalized distance of the projected point to the center of the band amounts to the sine of the angle  $\phi$ . In order to compute the sine, one of the two equalities below can be used:

$$|\sin(\phi)| = ||v' \times n||_2 = \sqrt{1 - \langle v', n \rangle^2}$$
 (1)

These statements hold due to the following mathematical properties of the sine, cosine, cross product and scalar product.

$$||v'||_{2} = ||n||_{2} = 1$$

$$\langle v', n \rangle = ||v'||_{2} ||n||_{2} \cos(\phi)$$

$$||v' \times n||_{2} = ||v'||_{2} ||n||_{2} |\sin(\phi)|$$

$$\sin^{2}(\phi) + \cos^{2}(\phi) = 1$$

$$\Rightarrow ||v' \times n||_{2} = |\sin(\phi)| = \sqrt{1 - \cos^{2}(\phi)} = \sqrt{1 - \langle v', n \rangle^{2}}$$
(2)

As a final step, the resulting distance  $|\sin(\phi)|$  needs to be corrected, as the absolute value of the sine doesn't go from 0 to 1 from one end of the imaginary band to the other, but from 1 to 0 in the middle and back to 1 at the other side. In order to correct this problem, we need to compute the sign of the sine by using the winding direction of the angle  $\phi$ . The sign of the sine can be computed as the sign of the volume of the parallelepiped spanned by t, v' and n.

$$vol(t, v', n) = det(t, v', n) = \langle t, v' \times n \rangle$$
 (3)

The equality of the determinant and the combination of the scalar product and cross product can be proven by simple expansion of the respective formulas using the three input vector coordinates as variables. Finally, we can compute the screen space band measure we are looking for as

$$d_{band} = \frac{1}{2}|\sin(\phi)| \cdot sgn(det(t, v', n)) + \frac{1}{2}.$$
 (4)

When mapping N parameters onto the tube, we subdivide the band position  $d_{band} \in (0,1)$  into multiple subband positions  $d_{sub}$ . For this, we compute the variable ID  $i_{var} = \lceil d_{band} \cdot N \rceil$  and then finally  $d_{sub} = d_{band} \cdot N - i_{var}$  (cf. Fig. 1).

### APPENDIX B GREAT CIRCLE-BASED SPHERE RENDERING

The spheres are drawn on the GPU using instanced rendering, where the sphere geometry is specified only once, and instantiated at all points where a sphere should be rendered. The pixel shader is then equipped with the following input variables.

- The fragment position  $p_{frag}$ .
- The surface normal n.
- The camera position  $p_{cam}$ .
- The trajectory entrance and exit points p<sub>a</sub> and p<sub>b</sub> computed as the first and last intersection of the trajectory with the sphere and their corresponding time steps t<sub>a</sub> and t<sub>b</sub>.

With this data, the view vector  $v=\frac{p_{cam}-p_{frag}}{\|p_{cam}-p_{frag}\|_2}$  and the trajectory direction vector  $l=\frac{p_b-p_a}{\|p_b-p_a\|_2}$  pointing from the entry point  $p_a$  into the direction of the exit point  $p_b$  can also be computed in the shader.

### B.1 Band Mapping on the Sphere

In order to compute which parameter band a fragment on the sphere belongs to, analogously to the tube, we propose to use the technique presented below. It solves different shortcomings compared to simply using the screen space location on the circular projection of the sphere (cf. Fig. 6 top compared to middle). If the entry and exit points are collinear with the center of the sphere, then a smooth transition between the color bands on the tube and the color bands on the sphere will be guaranteed independently of the viewing angle.

First, the projection of the sphere center  $p_{sphere}$  onto the surface of the sphere under the used camera transformation needs to be computed. For this, a ray-sphere intersection algorithm [1] is used with a ray starting at the camera position with direction  $p_{sphere}-p_{cam}$ , which yields the point  $p_{int}$ .

Next, the normal vectors of the two disks  $P_0$  spanned by the points  $(p_a, p_b, p_{int})$  and  $P_{frag}$  spanned by the points  $(p_a, p_b, p_{frag})$  are computed. The intersections of the disks with the sphere can be interpreted as two great circles meeting under a certain angle  $\theta$ .

Similarly to the tube surface, the value  $|sin(\theta)| = |n_0 \times n_{frag}||_2$  computed using the normal vectors of the two disks can be used as a measure in screen space for the distance to the border of the sphere. Finally, the band position is analogously given as

$$d_{band} = \frac{1}{2}|\sin(\theta)| \cdot sgn(det(l, n_0, n_{frag})) + \frac{1}{2}.$$
 (5)

When mapping N parameters onto the sphere, we again subdivide the band position  $d_{band} \in (0,1)$  into multiple sub-band positions  $d_{sub}$  (cf. Fig. 3).

A black separator line is drawn between two neighboring sub-bands. A problem that arises is that changes in the sub-band position and the direction orthogonal to it are no longer linear in screen space, especially when the sphere is viewed under an oblique angle, and thus distortions can occur. In the three subsections below, this problem and its solution are outlined. Using the correction factors

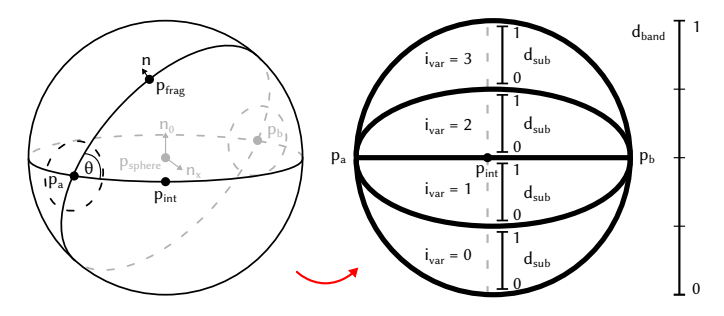


Fig. 3. Illustration of how the input vectors and points on the sphere are used to compute the band position  $d_{band}$ , the sub-band position  $d_{sub}$  and its corresponding variable ID  $i_{var}$ .

 $f_i$  introduced below, the final separator thickness can be computed as

$$w_{sep}' = \frac{w_{sep}}{f_1 f_2 f_3}. (6)$$

#### B.1.1 Lateral Band Thickness

In Equation 5, the sine of the angle  $\theta$  is used. However, if we look at the sphere from a direction that is not perpendicular to the vector connecting the entry and exit points, the problem arises that the sine of the angle of the two great circles is no longer a linear measure in screen space. The closer we get to the edge of the sphere, the higher the distortion. If we were to use the angle  $\theta$  directly instead of its sine, then the view dependent distortion disappears. Thus, the thickness is corrected using the derivative of the arcsine  $\frac{\partial \arcsin x}{\partial x} = \frac{1}{\sqrt{1-x^2}}$  with  $x = \|n_0 \times n_{frag}\|_2$ , i.e.,

$$f_1 = \frac{1}{\sqrt{1 - \|n_0 \times n_{frag}\|_2^2}}. (7)$$

### B.1.2 Longitudinal Band Thickness

Another problem is that the separator line gets thinner the closer it gets to the entrance and exit points (cf. Fig. 5 middle left). For the derivation of the formula below, it is assumed that the entrance and exit points are poles of the sphere, which is equivalent to assuming they are collinear with the sphere center. In all other cases, the distortion on the sphere surface will increase the sharper the angle  $\angle(p_a, p_{sphere}, p_b)$  between center and entry and exit point is. However, as sharp  $180^\circ$  turns in trajectory lines are very rare, this distortion will usually only be minor and won't impede the visualization strongly under normal circumstances.

For computing the correction factor  $f_2$ , the angular distance of the point  $p_{frag}$  from the point  $p_x$  in radians  $d_x = arccos(\langle p_x - p_{sphere}, p_{frag} - p_{sphere} \rangle)$  becomes necessary (cf. Fig. 4). We compute the angular distance  $d = \min(d_a, d_b)$  from one of the poles, and correspondingly the angular distance in radians  $\phi = \frac{\pi}{2} - d$  from the equator. The lateral radius of the sphere at  $p_{frag}$  is given as  $r \cdot \cos \phi$ , and consequentially, our final longitudinal band thickness correction factor amounts to

$$f_2 = \frac{r \cdot \cos \phi}{r} = \cos \phi. \tag{8}$$

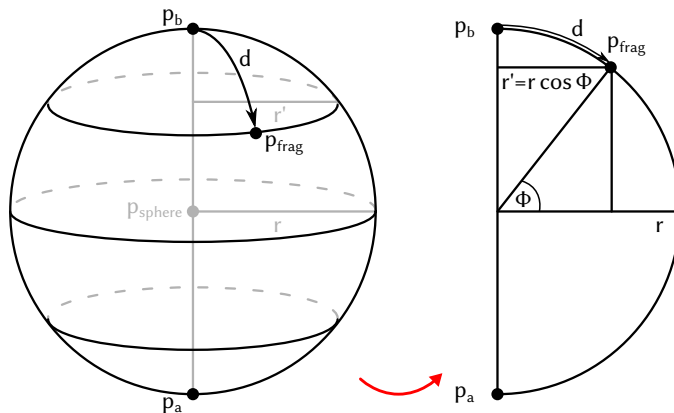


Fig. 4. Illustration of how the input points and vectors are used to compute the band position  $d_{band}$ , the sub-band position  $d_{sub}$  and its corresponding variable ID  $i_{var}$ .

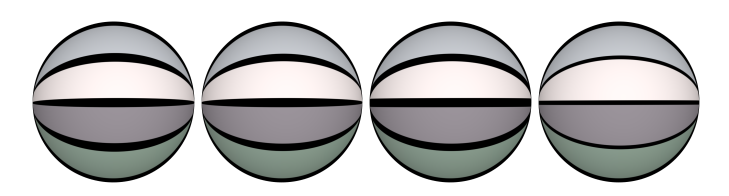


Fig. 5. From left to right: The effect of no correction factor and the three factors presented in subsubsection B.1.1, subsubsection B.1.2 and subsubsection B.1.3. Please note that the difference of the two leftmost spheres is hardly visible, as this type of distortion only appears when the sphere is viewed from an oblique angle not perpendicular to  $\ell$ .

#### B.1.3 Sphere Band Thickness

In order to achieve equal sub-band separator thickness of a sphere with its corresponding tube, a final correction factor is used. For example, if the diameter of the sphere 2r is twice the width of the tube  $w_{tube}$ , then the separator width in sub-band space will be halved using the factor below (cf. Fig. 5 right).

$$f_3 = \frac{2r}{w_{tube}} \tag{9}$$

### **B.2** Time Dimension Mapping on the Sphere

In order to map different time steps onto the sphere, the point closest to  $p_{frag}$  on the line segment  $(p_a,p_b)$  connecting the entry and exit point is computed. The distance of this point to  $p_a$  and  $p_b$  is then used to linearly interpolate between the time steps  $t_a$  and  $t_b$  at the entry and exit point to get the time step  $t_{frag}$  used for the fragment on the sphere surface. Then,  $t_{frag}$  is used to look up the parameter values of the trajectory at time step  $t_{frag}$  from a shader storage buffer stored on the GPU.

### APPENDIX C PIE CHART-BASED SPHERE RENDERING

For the rendering of a sphere colored via a pie charts, we want to subdivide the screen projection of the sphere in angular bands, i.e., individual pie slices (cf. Fig. 7). For this, we want to compute the angle  $\alpha_{band}$ , which represents the angular distance of the fragment  $p_{frag}$  to the up-axis of the camera. As input, we need the surface normal vector n, the camera view direction v and the camera up-vector up. As a

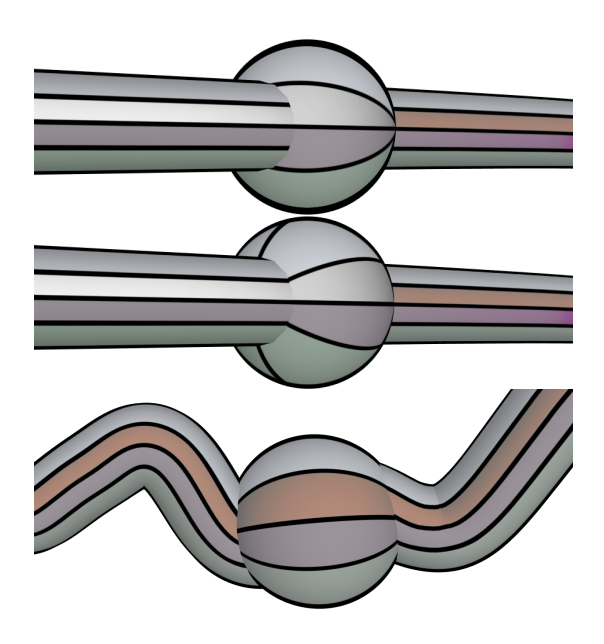


Fig. 6. Top: The rejected method using the pure screen space location on the circular projection of the sphere. Middle: Illustration of the smooth transition between tube bands and sphere bands when  $p_a,\ p_b$  and  $p_{sphere}$  are collinear. Bottom: Illustration of the hard transition between tube bands and sphere bands when  $p_a,\ p_b$  and  $p_{sphere}$  are not collinear. This effect can be observed at turns in the trajectory data.

first step, the normal  $\boldsymbol{n}$  is projected into the view plane to obtain

$$n_{proj} = n - \langle n, v \rangle \cdot n. \tag{10}$$

Then, we set  $n'=\frac{n_{proj}}{\|n_{proj}\|_2}$ . The length  $\|n_{proj}\|_2$  is the normalized screen space distance to the center of the sphere. This can be easily checked for the special case  $v=(0,0,1)^T$ , where  $\|n_{proj}\|_2$  becomes  $\sqrt{n_x^2+n_y^2}\in[0,1)$ . We will use this fact later in Equation 14. In the next step, we compute the angle  $\alpha_{band}$  as follows:

$$\alpha_{band} = atan2(det(n', up, v), \langle n', up \rangle) + \frac{\pi}{2}.$$
 (11)

atan2(y, x) computes the angle between the positive x axis and the line connecting the origin and the point  $(x, y)^T$ . atan2 returns the angle in mathematically positive direction, i.e., a counterclockwise angle. However, in our case, we do not want the counterclockwise angle to the positive x axis, but the clockwise angle from the positive y axis (the positive y axis being the up vector of the camera). This can be most easily achieved by transposing (i.e., interchanging) the x and y coordinates we feed to atan2. To get the y coordinate of the point we use for calculating the angle, the term  $\langle n', up \rangle$  is used in Equation 11. This way, we project the view plane normal onto the up axis vector. For the x coordinate, det(n', up, v) is used. We can again use Equation 3 to get the equality  $det(n', up, v) = \langle n', up \times v \rangle$ . Here,  $up \times v$  can be interpreted as the right axis vector of the view plane. When we project the view plane normal onto this new right axis vector, we get the x coordinate for Equation 11. The pie chart in the view plane can be seen in Fig. 7.

Finally, we can compute the global band position  $d_{band}$  as

$$d_{band} = \frac{\alpha_{band} \bmod 2\pi}{2\pi}.$$
 (12)

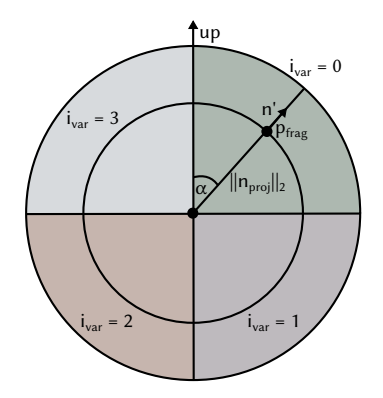


Fig. 7. Illustration of how the input vectors and points on the sphere are used to compute the band position  $d_{band}$ , the sub-band position  $d_{sub}$  and its corresponding variable ID  $i_{var}$ .

When mapping N parameters onto the sphere, we again subdivide the band position  $d_{band} \in [0,1)$  into multiple subband positions  $d_{sub}$  (cf. Fig. 7).

A black separator line is drawn between two neighboring sub-bands. A problem that also arises for the pie chart-based spheres is that changes in the sub-band position are not linear in screen space and dependent on the distance to the screen space center of the sphere. Consequently, two more correction factors are introduced below, and the final separator thickness is computed as

$$w'_{sep} = \frac{w_{sep}}{f_4 f_5}. (13)$$

The factor  $f_4$  is equal to  $||n_{proj}||_2$ , which itself, as was shown earlier in this section, is equal to the normalized distance to the screen space center of the sphere. This way, it is guaranteed that the separator thickness doesn't get thinner the closer we get to the center of the pie chart.

$$f_4 = ||n_{proj}||_2 \tag{14}$$

Finally, the factor  $f_5$  is used to make sure that the separator thickness of the pie chart sphere and the trajectory tube is equal. This time, we use the factor  $2r\pi$  in the numerator as opposed to 2r for the sphere bands, as our measure should no longer be relative to the diameter of the screen space circle/sphere, but its circumference.

$$f_5 = \frac{2r\pi}{w_{tube}} \tag{15}$$

### APPENDIX D VARIABLE AND PARAMETER NAMES

TABLE 1 Variable Names in the Dataset

Variable	Description
pressure	Pressure in hPa
Ť	Temperature in Kelvin
w	Vertical velocity in m s <sup>-1</sup>
S	Saturation
QV	Water vapor mass density in $kg m^{-3}$
QC	Cloud mass density in kg m <sup>-3</sup>
QR	Rain mass density in kg m <sup>-3</sup>
QS	Snow mass density in kg m <sup>-3</sup>
QI	Ice mass density in $kg m^{-3}$
QG	Graupel mass density in kg m $^{-3}$
QH	Hail mass density in $kg m^{-3}$
NCCLOUD	Cloud number density in m <sup>-3</sup>
NCRAIN	Rain number density in $m^{-3}$
NCSNOW	Snow number density in $m^{-3}$
NCICE	Ice number density in $m^{-3}$
NCGRAUPEL	Graupel number density in m <sup>-3</sup>
NCHAIL	Hail number density in $m^{-3}$
QR_OUT	Sedimentation of rain mass density out of the air
	parcel in kg m $^{-3}$
QS_OUT	Sedimentation of snow mass density out of the air
	parcel in $kg m^{-3}$
QI_OUT	Sedimentation of ice mass density out of the air
OC OUT	parcel in kg m <sup>-3</sup>
QG_OUT	Sedimentation of graupel mass density out of the
QH_OUT	air parcel in kg m <sup>-3</sup> Sedimentation of hail mass density out of the air
Qn_out	parcel in kg m $^{-3}$
NR_OUT	Sedimentation of rain number density out of the
TVK_OOT	air parcel in m <sup>-3</sup>
NS_OUT	Sedimentation of snow number density out of the
	air parcel in $m^{-3}$
NI_OUT	Sedimentation of ice number density out of the air
	parcel in $m^{-3}$
NG_OUT	Sedimentation of graupel number density out of
	the air parcel in $m^{-3}$
NH_OUT	Sedimentation of hail number density out of the
1-1	air parcel in m <sup>-3</sup>
latent_heat	Latent heat released by cloud microphysical pro-
latent_cool	cesses in J kg <sup>-1</sup> Latent heat absorbed by cloud microphysical pro-
laterit_coor	cesses in J kg <sup>-1</sup>
z	Height in m
Inactive	Number of nuclei that can not be activated for ice,
nactive	snow, graupel or hail
deposition	Mass density of water vapor deposited in ice,
-	snow, graupel and hail
sublimination	Mass density of water vapor from ice, snow, grau-
	pel and hail
time_after_ascent	Time centered to the start of the fastest ascent in a
400	2h time window
conv_400	Flag for a convective ascent of 400 hPa
conv_600	Flag for a convective ascent of 600 hPa
slan_400	Flag for a slantwise ascent of 400 hPa
slan_600	Flag for a slantwise ascent of 600 hPa
step	Simulation step
phase	Flag for different phases of the trajectory. 0: warm phase, 1: mixed phase, 2: ice phase, 3: neutral
	phase 1. Illixed phase, 2. Ice phase, 3. Heutral
	1 Primot

TABLE 2 Parameter Names in the Dataset

Parameter	Description
inv_z	Inverse of air parcel size (height) used in explicit
	sedimentation) (cf. [2])
rho_vel	Exponent for density correction (cf. [3], Eq. (33))
D_rainfrz_gh	Size threshold for partitioning of freezing rain in the hail scheme (cf. [3])
p_sat_melt	Saturation pressure at $T = 273.15 \text{ K (cf. [3])}$
a_HET	Exponent for heterogeneous rain freezing with data of Barklie and Gokhale (cf. [3])
k_r	Coefficient for accretion of QC to QR (cf. [3])
a_ccn_1	Parameter for CCN concentration (cf. [4])
a_ccn_4	Parameter for CCN concentration (cf. [4])
b_ccn_1	Parameter for CCN concentration (cf. [4])
b_ccn_3	Parameter for CCN concentration (cf. [4])
b_ccn_4	Parameter for CCN concentration (cf. [4])
c_ccn_1	Parameter for CCN concentration (cf. [4])
c_ccn_3	Parameter for CCN concentration (cf. [4])
c_ccn_4	Parameter for CCN concentration (cf. [4])
d_ccn_1	Parameter for CCN concentration (cf. [4])
d_ccn_2	Parameter for CCN concentration (cf. [4])
d_ccn_3	Parameter for CCN concentration (cf. [4])
d_ccn_4	Parameter for CCN concentration (cf. [4])
rain_a_geo	Coefficient for diameter size calculation (cf. [3] Eq. (32))
rain_b_geo	Exponent for diameter size calculation (cf. [3] Eq. (32))
rain_min_x	Minimum size of the particle used after the microphysics (cf. [3], Eqs. (94), (97))
rain_a_vel	Coefficient for particle velocity (cf. [3] Eq. (33))
rain_b_vel	Exponent for particle velocity (cf. [3] Eq. (33))
rain_alpha	Constant in rain sedimentation (cf. [5], Eq. (A10))
rain_beta	Coefficient for rain sedimentation (cf. [5], Eq. (A10))
rain_gamma	Exponent for rain sedimentation (cf. [5], Eq. (A10))
rain_nu	Parameter to calculate the shape of the generalized $\Gamma$ -distribution (cf. [3], Eq. (79))
rain_mu	Shape parameter of the generalized $\Gamma$ -distribution (cf. [3], Eq. (79))
graupel_a_geo	Coefficient for diameter size calculation (cf. [3] Eq. (32))
graupel_b_geo	Exponent for diameter size calculation (cf. [3] Eq. (32))
graupel_a_vel	Coefficient for particle velocity (cf. [3] Eq. (33))
graupel_b_vel	Exponent for particle velocity (cf. [3] Eq. (33))
graupel_vsedi_max	Maximum sedimentation velocity parameter (cf. [2])
ice_a_geo	Coefficient for diameter size calculation (cf. [3] Eq. (32))
ice_b_geo	Exponent for diameter size calculation (cf. [3] Eq. (32))
ice_b_vel	Exponent for particle velocity (cf. [3] Eq. (33))
ice_vsedi_max	Maximum sedimentation velocity parameter (cf. [2])
snow_b_geo	Exponent for diameter size calculation (cf. [3] Eq. (32))
snow_b_vel	Exponent for particle velocity (cf. [3] Eq. (33))
snow_vsedi_max	Maximum sedimentation velocity parameter (cf. [2])
	[ <del>-</del> ]/

## APPENDIX E REGIONS AND TIMES OF INTEREST SELECTION FOR CASE-STUDY "VLADIANA"

Section 6 of our work gives an example for investigating the rain mass density (QR) along WCB trajectories within "Vladiana", focusing on the joint development of multiple model parameter sensitivities. In this section, we demonstrate how our domain scientists identify regions and times of interest using our exploratory visual analysis capabilities. The different steps in this process are described below.

Trajectories initialized at similar time steps and regions may show different behavior responsible for diverse cloud structures and precipitation patterns. With Met.3D, one can identify such coherent clusters of trajectories and their characteristics. As a first step, we load a sample of 50 preselected trajectories from our trajectory dataset and select all to see the curve plot. Fig. 8 shows a clear peak of rain mass density (QR) that we will investigate. We select the time step of the peak in QR and select all trajectories that contribute to the peak around this time step. For this, we click all trajectories where the sphere shows no blue segment to deselect them, see Fig. 9. To visualize the characteristics, we sort the similarity of the curve plot by QR, see Fig. 9. These trajectories have similar times of ascent (compare pressure evolution), and precipitation occurs before cloud formation starts in these trajectories, i.e., rainfall sediments into the ascending WCB air from cloud layers above its current position. The ascent of a trajectory is usually accompanied by cloud formation and then precipitation. One may further assume that trajectories started at similar areas and times have identical characteristics. To check this assumption, we go to the initial time step and select trajectories in a similar region. The right group in Fig. 10 are three trajectories we selected in addition. The curve plot reveals the different ascent times (early blue high-variance area in curve-plot pressure) and earlier cloud formation (new peaks in QC). We discovered two sets of trajectories: One involves large precipitation rates and another set with strong cloud formation at an earlier time and in a different area. Based on the identified characteristics, we can filter our dataset for more similar trajectories and investigate them as a whole.

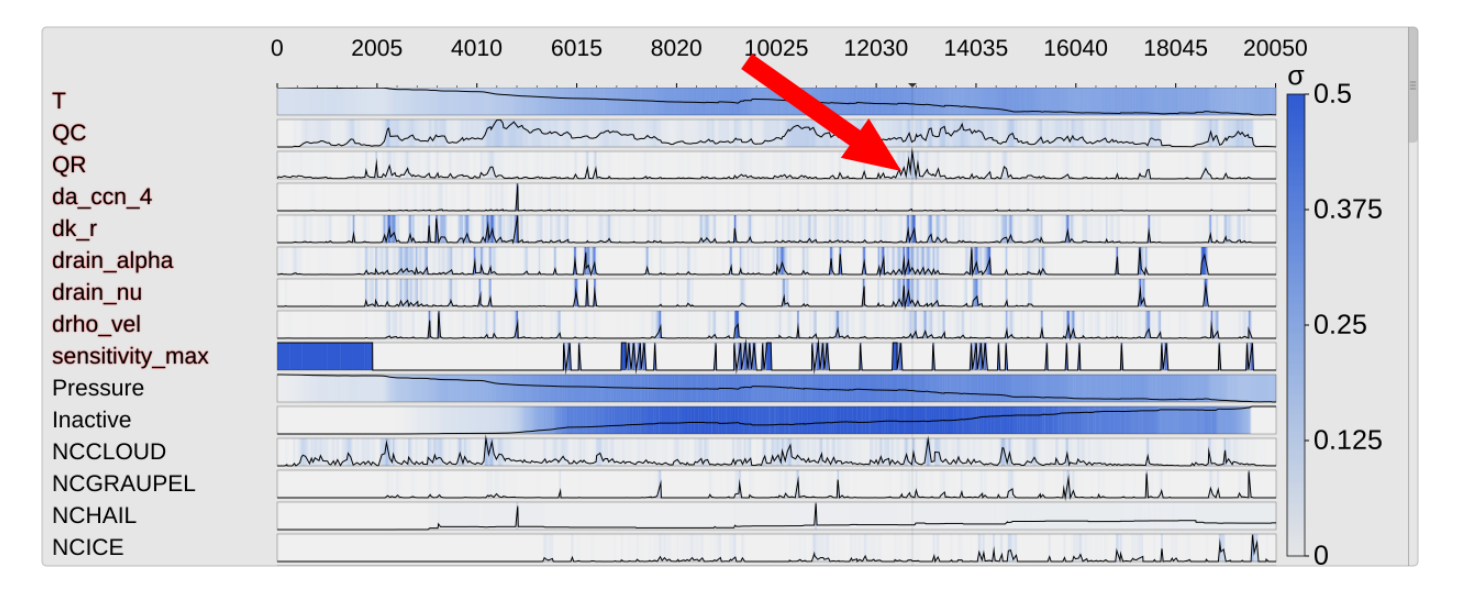


Fig. 8. Concentrating on rain mass density (QR), we use the curve plot to look for time steps with extreme values worth further investigation. Such a selection can be made with multiple variables or sensitivities in mind.

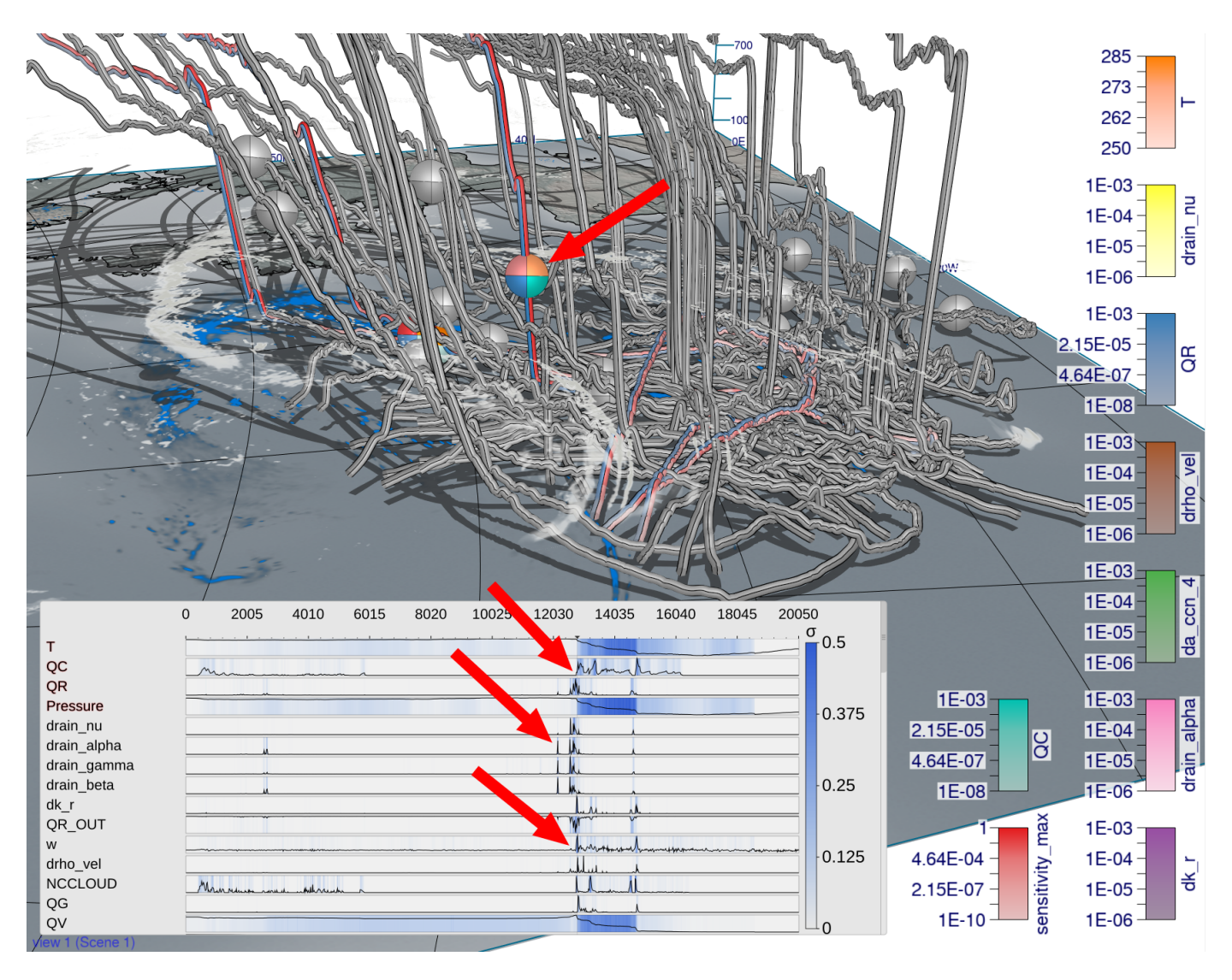


Fig. 9. Using the spheres, we select the trajectories that contribute to the peak previously identified. The blue segment of the sphere corresponds to high rain mass density. Once all trajectories in question are selected, the curve plots are sorted by similarity to rain mass density. Comparing the location of the peaks in rain mass density with peaks in sensitivities reveals that activation of precipitation processes coincides with increased rain mass. In contrast, cloud formation indicated by QC starts afterwards and coincides with rising levels of the trajectories given by pressure.

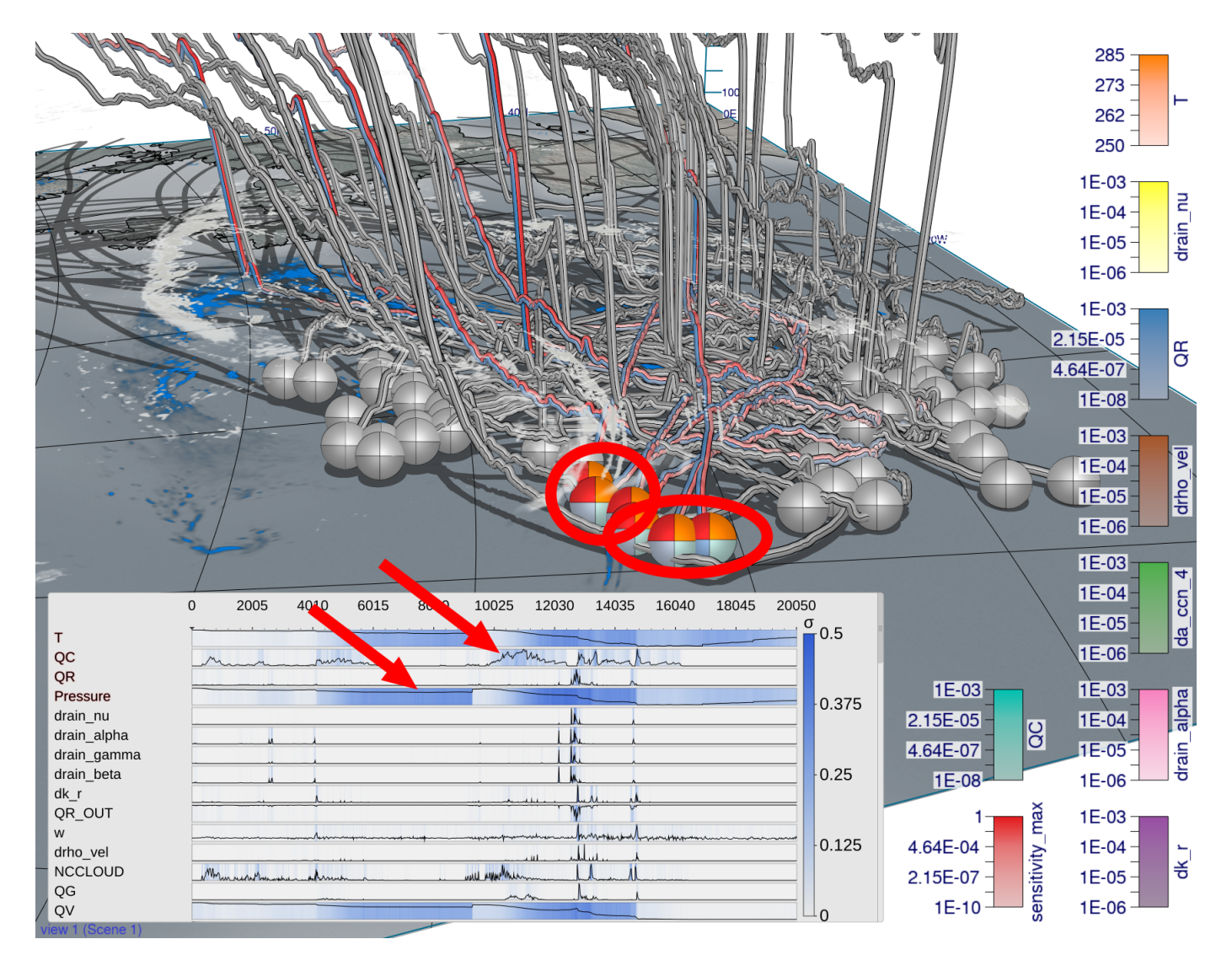


Fig. 10. By changing the time step, we can trace the origin of the selected trajectories (left group). Several more trajectories in that area have not been selected previously (right group). We select the other trajectories to assess the difference between the initially chosen trajectories and the new ones with the same origin. The newly selected trajectories ascend earlier than before, albeit in a similar region. Furthermore, the curve plots clearly show an early cloud formation via QR and the large variance in ascent time given by the blue shade in pressure.

### APPENDIX F USER STUDY TASKS

In Fig. 11, Fig. 12 and Fig. 13, we show representative images from the user study for task T1, T2 and T3, respectively. The problem statements users were asked to solve with respect to these images were as follows.

- 1) T1: "Which trajectories are outliers with respect to their multi-parameter distribution at the selected time step?"
- 2) T2: "Which trajectories have the most similar distributions of quantities to the target distribution at the top?"
- 3) T3: "Group the trajectories into two clusters by the similarity of their multi-parameter distributions at the selected time step."

Whether participants were presented an image using bands-based or pie charts-based focus spheres was randomized. Each user got the same number of images for each visual mapping.

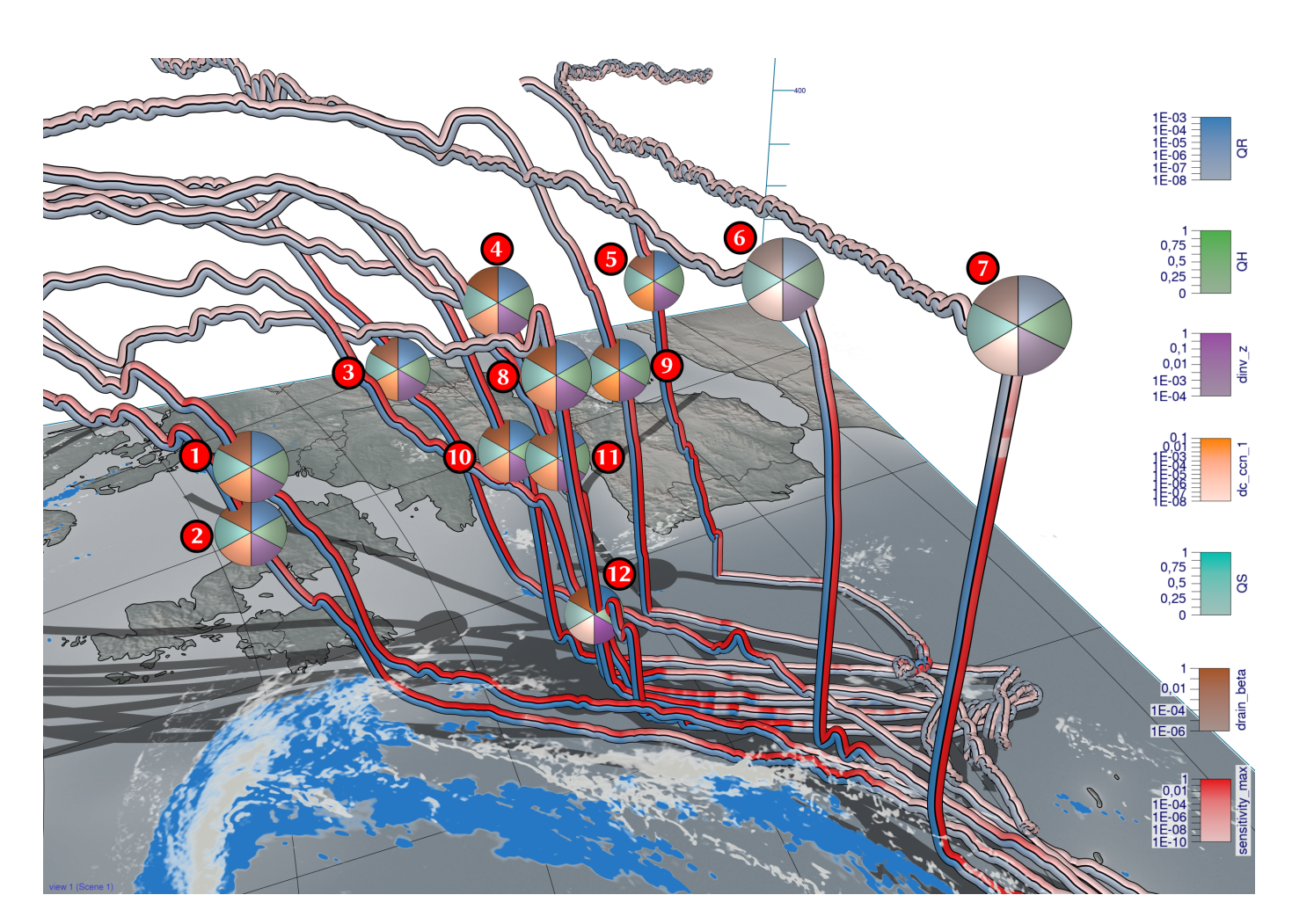


Fig. 11. Representative image for user study task T1. Users needed to find trajectories which behave against the trend at the selected time step.

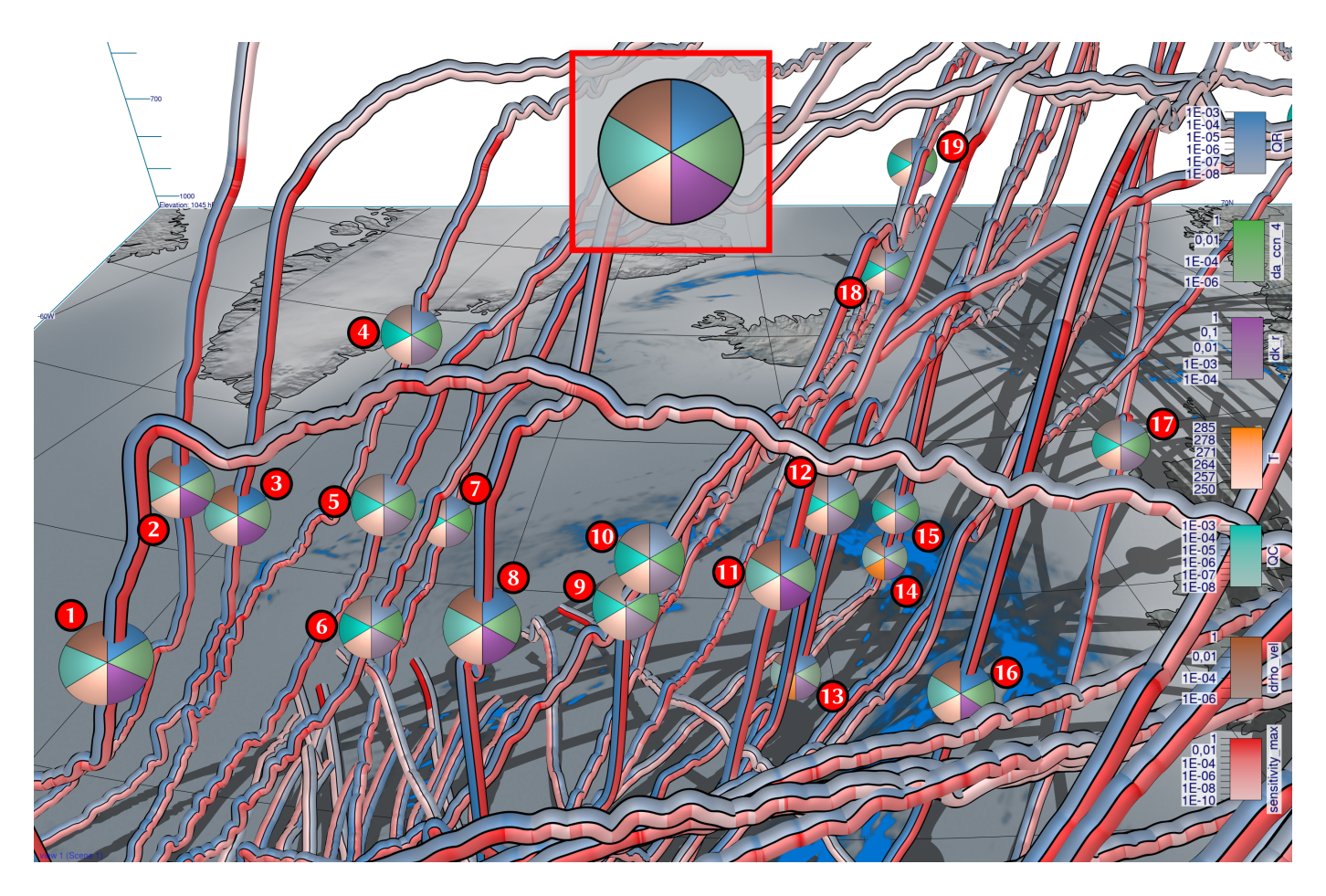


Fig. 12. Representative image for user study task T2. Users needed to find trajectories with multi-parameter distributions similar to the reference distribution.

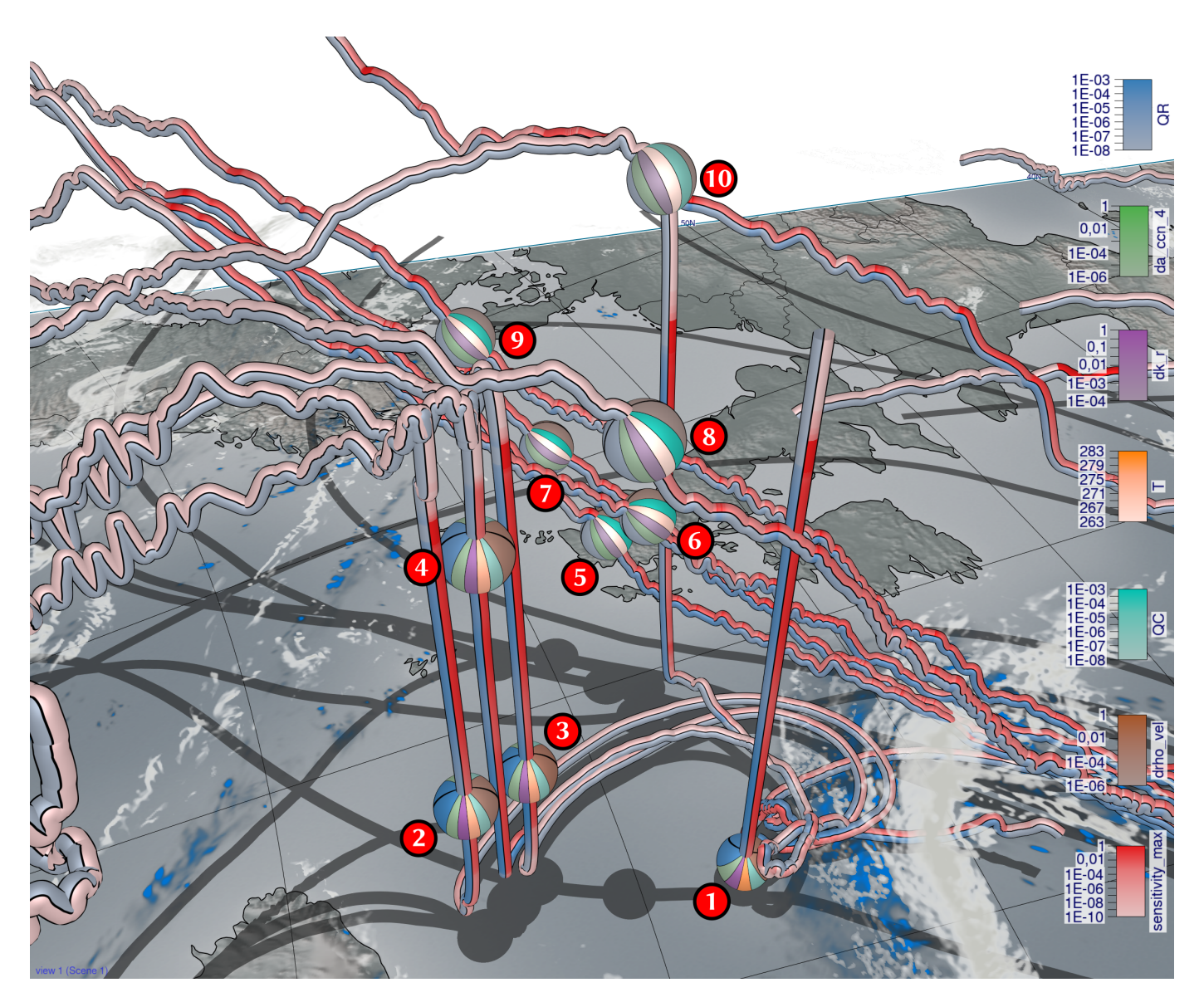


Fig. 13. Representative image for user study task T3. Participants needed to assign trajectories with similar multi-parameter distributions to the same cluster.

### **APPENDIX G**

### VISUALIZATION USING DISCRETE COLOR MAPS

In Fig. 14, we demonstrate the use of discrete, quantized 8-class single hue color maps from ColorBrewer [6]. Using quantized color maps, it can be easier to assign colors on the trajectories and bands to individual values in the color maps.

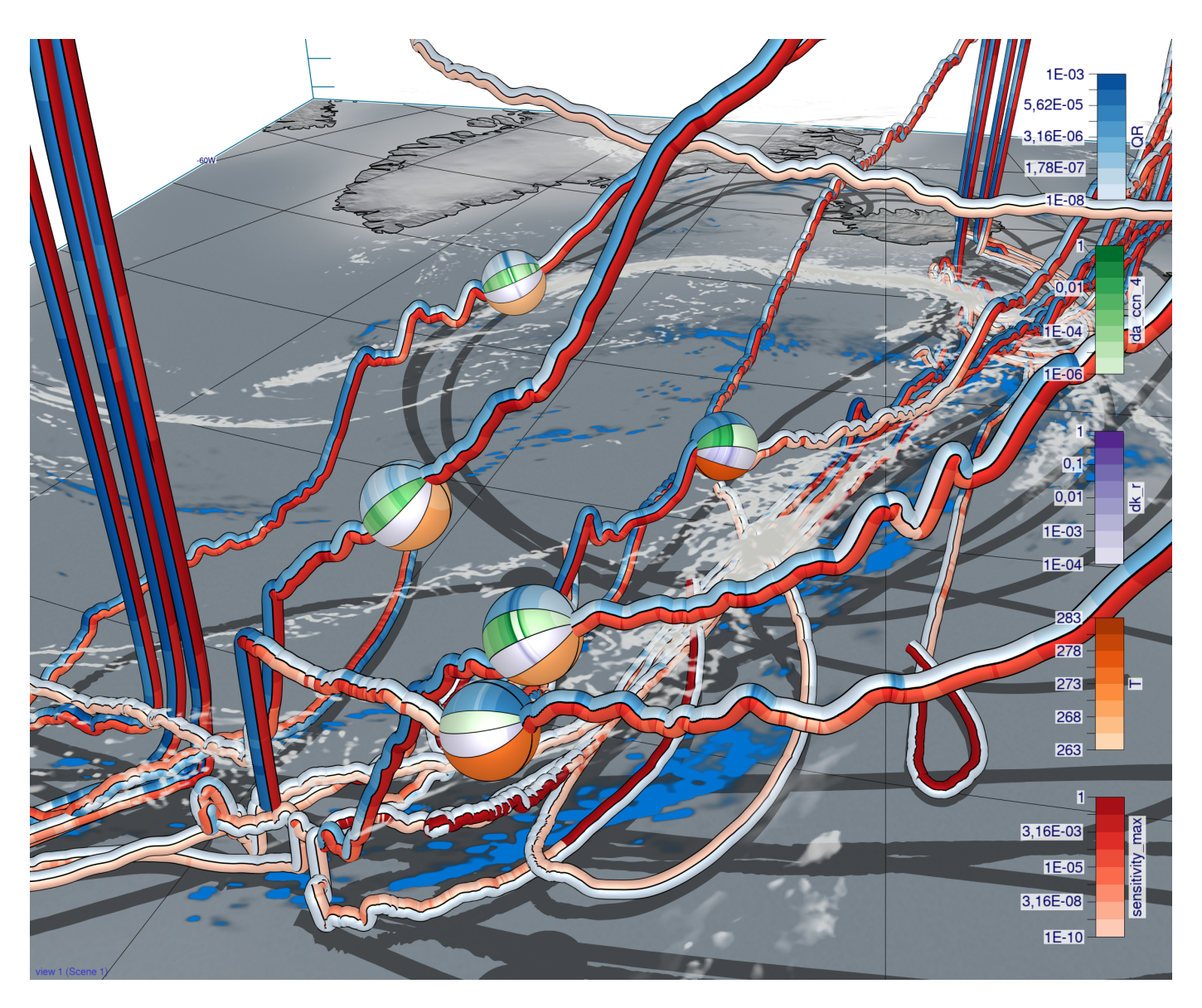


Fig. 14. Visualization using discrete, quantized 8-class single hue color maps from ColorBrewer.

### **ACKNOWLEDGMENTS**

The authors acknowledge support by the Deutsche Forschungsgemeinschaft (DFG) within the Transregional Collaborative Research Centre TRR165 Waves to Weather, (www.wavestoweather.de), Projects A7, Z2 and B8 as well as funding from JGU Mainz.

#### REFERENCES

- [1] S. Owen, "Hypergraph ray-sphere intersection," https://education.siggraph.org/static/HyperGraph/raytrace/ rtinter1.htm, 1999, accessed: 2022-02-09.
- [2] M. Hieronymus, "Algorithmic differentiation for sensitivity analysis in cloud microphysics (v2.1)," 2022.
- [3] A. Seifert and K. D. Beheng, "A two-moment cloud microphysics parameterization for mixed-phase clouds. part 1: Model description," *Meteorol. Atmos. Phys.*, vol. 92, no. 1, pp. 45–66, 2006.
  [4] L. B. Hande, C. Engler, C. Hoose, and I. Tegen, "Parameterizing
- [4] L. B. Hande, C. Engler, C. Hoose, and I. Tegen, "Parameterizing cloud condensation nuclei concentrations during HOPE," *Atmos. Chem. Phys.*, vol. 16, no. 18, pp. 12059–12079, 2016.
  [5] A. Seifert, "On the parameterization of evaporation of raindrops
- [5] A. Seifert, "On the parameterization of evaporation of raindrops as simulated by a one-dimensional rainshaft model," *J. Atmos. Sci*, vol. 65, no. 11, pp. 3608–3619, 2008.
- [6] M. Harrower and C. A. Brewer, "Colorbrewer.org: An online tool for selecting colour schemes for maps," *The Cartographic Journal*, vol. 40, no. 1, pp. 27–37, 2003. [Online]. Available: https://www.tandfonline.com/doi/abs/10.1179/000870403235002042



Christoph Neuhauser is a PhD candidate at the Computer Graphics and Visualization Group at the Technical University of Munich (TUM). He received his Bachelor's and Master's degrees in computer science from TUM in 2019 and 2020. Major interests in research comprise scientific visualization and real-time rendering.



Maicon Hieronymus is a PhD candidate at the Efficient Computing and Storage Group at the Johannes Gutenberg University Mainz (JGU) since 2019. He studied computer science (B.Sc.) and computer science with minor in physics (M.Sc.) at JGU. Research interests involve model analysis of cloud microphysical models and algorithmic differentiation in atmospheric physics.



Michael Kern is a research scientist and software engineer at Advanced Micro Devices (AMD) with major focus on real-time computer graphics and ray tracing. He studied computer science and received his Ph.D. from TUM in 2020. His thesis was concerned about feature detection and uncertainty visualization in meteorological data. Besides work, his main interests are scientific visualization and high-performance GPU computing.



Marc Rautenhaus received the M.Sc. degree in atmospheric science from the University of British Columbia, Vancouver, in 2007, and the Ph.D. degree in computer science from TUM, Munich, in 2015. He currently leads the Visual Data Analysis Group at the Regional Computing Centre of Universität Hamburg. Marc's research interests focus on the intersection of visualization, data analysis, and meteorology.



Annika Oertel Annika Oertel studied atmospheric science and received a Ph.D. in atmospheric dynamics from ETH Zurich. Since 2020 she works as postdoctoral researcher in the Institute of Meteorology and Climate Research at Karlsruhe Institute of Technology. Her research focuses on the model representation of microphysical processes in warm conveyor belts and their interactions with the larger-scale extratropical circulation.



**Rüdiger Westermann** studied computer science at the Technical University Darmstadt and received his Ph.D. in computer science from the University of Dortmund, both in Germany. In 2002, he was appointed the chair of Computer Graphics and Visualization at TUM. His research interests include scalable data visualization and simulation algorithms, GPU computing, real-time rendering of large data, and uncertainty visualization.